

# MRS: A FAST SAMPLER FOR MEAN REVERTING DIFFUSION BASED ON ODE AND SDE SOLVERS

000  
001  
002  
003  
004  
005 **Anonymous authors**  
006 Paper under double-blind review  
007  
008  
009  
010

## ABSTRACT

011 In applications of diffusion models, controllable generation is of practical significance,  
012 but is also challenging. Current methods for controllable generation primarily focus on modifying the score function of diffusion models, while Mean  
013 Reverting (MR) Diffusion directly modifies the structure of the stochastic differential equation (SDE), making the incorporation of image conditions simpler and  
014 more natural. However, current training-free fast samplers are not directly applicable to MR Diffusion. And thus MR Diffusion requires hundreds of NFEs  
015 (number of function evaluations) to obtain high-quality samples. In this paper,  
016 we propose a new algorithm named MRS (MR Sampler) to reduce the sampling  
017 NFEs of MR Diffusion. We solve the reverse-time SDE and the probability flow  
018 ordinary differential equation (PF-ODE) associated with MR Diffusion, and derive  
019 semi-analytical solutions. The solutions consist of an analytical function and  
020 an integral parameterized by a neural network. Based on this solution, we can generate  
021 high-quality samples in fewer steps. Our approach does not require training  
022 and supports all mainstream parameterizations, including noise prediction, data  
023 prediction and velocity prediction. Extensive experiments demonstrate that MR  
024 Sampler maintains high sampling quality with a speedup of 10 to 20 times across  
025 ten different image restoration tasks. Our algorithm accelerates the sampling pro-  
026 cedure of MR Diffusion, making it more practical in controllable generation.  
027  
028  
029  
030

## 1 INTRODUCTION

031 Diffusion models have emerged as a powerful class of generative models, demonstrating remarkable  
032 capabilities across a variety of applications, including image synthesis (Dhariwal & Nichol, 2021;  
033 Ruiz et al., 2023; Rombach et al., 2022) and video generation (Ho et al., 2022a;b). In these applications,  
034 controllable generation is very important in practice, but it also poses considerable challenges.  
035 Various methods have been proposed to incorporate text or image conditions into the score function  
036 of diffusion models(Ho & Salimans, 2022; Ye et al., 2023; Zhang et al., 2023), whereas Mean Revert-  
037 ing (MR) Diffusion offers a new avenue of control in the generation process (Luo et al., 2023b).  
038 Previous diffusion models (such as DDPM (Ho et al., 2020)) simulate a diffusion process that grad-  
039 ually transforms data into pure Gaussian noise, followed by learning to reverse this process for  
040 sample generation (Song & Ermon, 2020; Song et al., 2021). In contrast, MR Diffusion is designed  
041 to produce final states that follow a Gaussian distribution with a non-zero mean, which provides  
042 a simple and natural way to introduce image conditions. This characteristic makes MR Diffusion  
043 particularly suitable for solving inverse problems and potentially extensible to multi-modal condi-  
044 tions. However, the sampling process of MR Diffusion requires hundreds of iterative steps, which is  
045 time-consuming.

046 To improve the sampling efficiency of diffusion models, various acceleration strategies have been  
047 proposed, which can be divided into two categories. The first explores methods that establish di-  
048 rect mappings between starting and ending points on the sampling trajectory, enabling acceleration  
049 through knowledge distillation (Salimans & Ho, 2022; Song et al., 2023; Liu et al., 2022b). However,  
050 such algorithms often come with trade-offs, such as the need for extensive training and limitations  
051 in their adaptability across different tasks and datasets. The second category involves the design of  
052 fast numerical solvers that increase step sizes while controlling truncation errors, thus allowing for  
053 faster convergence to solutions (Lu et al., 2022a; Zhang & Chen, 2022; Song et al., 2020a).

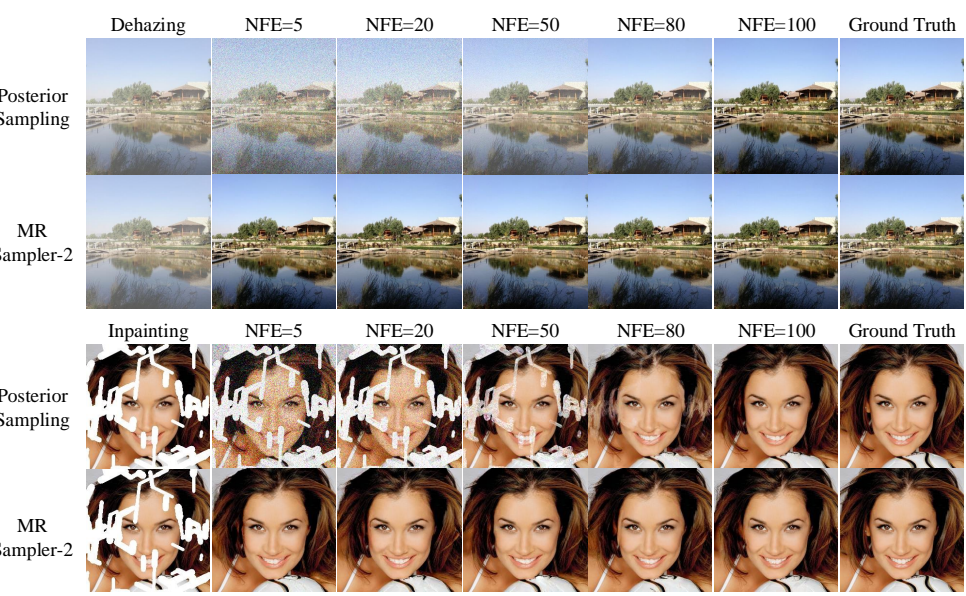


Figure 1: **Qualitative comparisons between MR Sampler and Posterior Sampling.** All images are generated by sampling from a pre-trained MR Diffusion (Luo et al., 2024a) on the RESIDE-6k (Qin et al., 2020b) dataset and the CelebA-HQ (Karras, 2017) dataset.

Notably, fast sampling solvers mentioned above are designed for common SDEs such as VPSDE and VESDE (Song et al., 2020b). Due to the difference between these SDEs and MRSDE, existing training-free fast samplers cannot be directly applied to Mean Reverting (MR) Diffusion. In this paper, we propose a novel algorithm named MRS (MR Sampler) that improves the sampling efficiency of MR Diffusion. Specifically, we solve the reverse-time stochastic differential equation (SDE) and probability flow ordinary differential equation (PF-ODE) (Song et al., 2020b) derived from MRSDE, and obtain a semi-analytical solution, which consists of an analytical function and an integral parameterized by neural networks. We prove that the difference of MRSDE only leads to change in analytical part of solution, which can be calculated precisely. And the integral part can be estimated by discretization methods developed in several previous works (Lu et al., 2022a; Zhang & Chen, 2022; Zhao et al., 2024). We derive sampling formulas for two types of neural network parameterizations: noise prediction (Ho et al., 2020; Song et al., 2020b) and data prediction (Salimans & Ho, 2022). Through theoretical analysis and experimental validation, we demonstrate that data prediction exhibits superior numerical stability compared to noise prediction. Additionally, we propose transformation methods for velocity prediction networks (Salimans & Ho, 2022) so that our algorithm supports all common training objectives. Extensive experiments show that our fast sampler converges in 5 or 10 NFEs with high sampling quality. As illustrated in Figure 1, our algorithm achieves stable performance with speedup factors ranging from 10 to 20.

In summary, our main contributions are as follows:

- We propose *MR Sampler*, a fast sampling algorithm for MR Diffusion, based on solving the PF-ODE and SDE derived from MRSDE. Our algorithm is plug-and-play and can adapt to all common training objectives.
- We demonstrate that posterior sampling (Luo et al., 2024b) for MR Diffusion is equivalent to Euler-Maruyama discretization, whereas MR Sampler computes a semi-analytical solution, thereby eliminating part of approximation errors.
- Through extensive experiments on ten image restoration tasks, we demonstrate that MR Sampler can reduce the required sampling time by a factor of 10 to 20 with comparable sampling quality. Moreover, we reveal that data prediction exhibits superior numerical stability compared to noise prediction.

108    **2 BACKGROUND**

110    In this section, we briefly review the basic definitions and characteristics of diffusion probabilistic  
 111    models and mean-reverting diffusion models.

113    **2.1 DIFFUSION PROBABILISTIC MODELS**

115    According to Song et al. (2020b), Diffusion Probabilistic Models (DPMs) can be defined as the  
 116    solution of the following Itô stochastic differential equation (SDE), which is a stochastic process  
 117     $\{\mathbf{x}_t\}_{t \in [0, T]}$  with  $T > 0$ , called *forward process*, where  $\mathbf{x}_t \in \mathbb{R}^D$  is a D-dimensional random variable.

$$d\mathbf{x} = f(\mathbf{x}, t)dt + g(t)d\mathbf{w}. \quad (1)$$

120    The forward process performs adding noise to the data  $\mathbf{x}_0$ , while there exists a corresponding reverse  
 121    process that gradually removes the noise and recovers  $\mathbf{x}_0$ . Anderson (1982) shows that the reverse  
 122    of the forward process is also a solution of an Itô SDE:

$$d\mathbf{x} = [f(\mathbf{x}, t) - g(t)^2 \nabla_{\mathbf{x}} \log p_t(\mathbf{x})]dt + g(t)d\bar{\mathbf{w}}, \quad (2)$$

125    where  $f$  and  $g$  are the drift and diffusion coefficients respectively,  $\bar{\mathbf{w}}$  is a standard Wiener process  
 126    running backwards in time, and time  $t$  flows from  $T$  to 0, which means  $dt < 0$ . The score function  
 127     $\nabla_{\mathbf{x}} \log p_t(\mathbf{x})$  is generally intractable and thus a neural network  $s_{\theta}(\mathbf{x}, t)$  is used to estimate it by  
 128    optimizing the following objective (Song et al., 2020b; Hyvärinen & Dayan, 2005):

$$\theta^* = \arg \min_{\theta} \mathbb{E}_t \left\{ \lambda(t) \mathbb{E}_{\mathbf{x}_0} \mathbb{E}_{\mathbf{x}_t | \mathbf{x}_0} \left[ \|s_{\theta}(\mathbf{x}_t, t) - \nabla_{\mathbf{x}_t} \log p(\mathbf{x}_t | \mathbf{x}_0)\|_2^2 \right] \right\}. \quad (3)$$

131    where  $\lambda(t) : [0, T] \rightarrow \mathbb{R}^+$  is a positive weighting function,  $t$  is uniformly sampled over  $[0, T]$ ,  
 132     $\mathbf{x}_0 \sim p_0(\mathbf{x})$  and  $\mathbf{x}_t \sim p(\mathbf{x}_t | \mathbf{x}_0)$ . To facilitate the computation of  $p(\mathbf{x}_t | \mathbf{x}_0)$ , the drift coefficient  
 133     $f(\mathbf{x}, t)$  is typically defined as a linear function of  $\mathbf{x}$ , as presented in Eq.(4). Based on the inference  
 134    by Särkkä & Solin (2019) in Section 5.5, the transition probability  $p(\mathbf{x}_t | \mathbf{x}_0)$  corresponding to Eq.(4)  
 135    follows Gaussian distribution, as shown in Eq.(5).

$$d\mathbf{x} = f(t)\mathbf{x}dt + g(t)d\mathbf{w}, \quad (4)$$

$$p(\mathbf{x}_t | \mathbf{x}_0) \sim \mathcal{N} \left( \mathbf{x}_t; \mathbf{x}_0 e^{\int_0^t f(\tau)d\tau}, \int_0^t e^{2 \int_{\tau}^t f(\xi)d\xi} g^2(\tau)d\tau \cdot \mathbf{I} \right). \quad (5)$$

140    Song et al. (2020b) proved that Denoising Diffusion Probabilistic Models (Ho et al., 2020) and  
 141    Noise Conditional Score Networks (Song & Ermon, 2019) can be regarded as discretizations of  
 142    Variance Preserving SDE (VPSDE) and Variance Exploding SDE (VESDE), respectively. As shown  
 143    in Table 1, the SDEs corresponding to the two most commonly used diffusion models both follow  
 144    the form of Eq.(4).

145    Table 1: Two popular SDEs, Variance Preserving SDE (VPSDE) and Variance Exploding SDE  
 146    (VESDE).  $m(t)$  and  $v(t)$  refer to mean and variance of the transition probability  $p(\mathbf{x}_t | \mathbf{x}_0)$ .

SDE	$f(t)$	$g(t)$	$m(t)$	$v(t)$
VPSDE(Ho et al., 2020)	$-\frac{1}{2}\beta(t)$	$\sqrt{\beta(t)}$	$\mathbf{x}_0 e^{-\frac{1}{2} \int_0^t \beta(\tau)d\tau}$	$\mathbf{I} - \mathbf{I} e^{-\int_0^t \beta(\tau)d\tau}$
VESDE(Song & Ermon, 2019)	0	$\sqrt{\frac{d[\sigma^2(t)]}{dt}}$	$\mathbf{x}_0$	$[\sigma^2(t) - \sigma^2(0)] \mathbf{I}$

154    **2.2 MEAN REVERTING DIFFUSION MODELS**

155    Luo et al. (2023b) proposed a special case of Itô SDE named Mean Reverting SDE (MRSDE), as  
 156    follows:

$$d\mathbf{x} = f(t)(\boldsymbol{\mu} - \mathbf{x})dt + g(t)d\mathbf{w}, \quad (6)$$

157    where  $\boldsymbol{\mu}$  is a parameter vector that has the same shape of variable  $\mathbf{x}$ , and  $f(t), g(t)$  are time-  
 158    dependent non-negative parameters that control the speed of the mean reversion and stochastic  
 159    volatility, respectively. To prevent potential confusion, we have substituted the notation used in

the original paper (Luo et al., 2023b). For further details, please refer to Appendix B. Under the assumption that  $g^2(t)/f(t) = 2\sigma_\infty^2$  for any  $t \in [0, T]$  with  $T > 0$ , Eq.(6) has a closed-form solution, given by

$$\mathbf{x}_t = \mathbf{x}_0 e^{-\int_0^t f(\tau) d\tau} + \boldsymbol{\mu}(1 - e^{-\int_0^t f(\tau) d\tau}) + \sigma_\infty \sqrt{1 - e^{-2 \int_0^t f(\tau) d\tau}} \mathbf{z}, \quad (7)$$

where  $\sigma_\infty$  is a positive hyper-parameter that determines the standard deviation of  $\mathbf{x}_t$  when  $t \rightarrow \infty$  and  $\mathbf{z} \sim \mathcal{N}(\mathbf{0}, \mathbf{I})$ . Note that  $\mathbf{x}_t$  starts from  $\mathbf{x}_0$ , and converges to  $\boldsymbol{\mu} + \sigma_\infty \mathbf{z}$  as  $t \rightarrow \infty$ . According to Anderson (1982)'s result, we can derive the following reverse-time SDE:

$$d\mathbf{x} = [f(t)(\boldsymbol{\mu} - \mathbf{x}) - g^2(t)\nabla_{\mathbf{x}} \log p_t(\mathbf{x})] dt + g(t)d\bar{w}. \quad (8)$$

Similar to DPMs, the score function in Eq.(8) can also be estimated by score matching methods Song & Ermon (2019); Song et al. (2021). Once the score function is known, we can generate  $\mathbf{x}_0$  from a noisy state  $\mathbf{x}_T$ . In summary, MRSDE illustrates the conversion between two distinct types of data and has demonstrated promising results in image restoration tasks (Luo et al., 2023c).

Various algorithms have been developed to accelerate sampling of VPSDE, including methods like CCDF (Chung et al., 2022), DDIM (Song et al., 2020a), PNDM (Liu et al., 2022a), DPM-Solver (Lu et al., 2022a) and UniPC (Zhao et al., 2024). Additionally, Karras et al. (2022) and Zhou et al. (2024) have introduced techniques for accelerating sampling of VESDE. However, the drift coefficient of VPSDE and VESDE is a linear function of  $\mathbf{x}$ , while the drift coefficient in MRSDE is an affine function w.r.t.  $\mathbf{x}$ , adding an intercept  $\boldsymbol{\mu}$  (see Eq.(4) and Eq.(6)). Therefore, current sampling acceleration algorithms cannot be applied to MR Diffusion. To the best of our knowledge, MR Sampler has been the first sampling acceleration algorithm for MR Diffusion so far.

### 3 FAST SAMPLERS FOR MEAN REVERTING DIFFUSION WITH NOISE PREDICTION

According to Song et al. (2020b), the states  $\mathbf{x}_t$  in the sampling procedure of diffusion models correspond to solutions of reverse-time SDE and PF-ODE. Therefore, we look for ways to accelerate sampling by studying these solutions. In this section, we solve the noise-prediction-based reverse-time SDE and PF-ODE, and we numerically estimate the non-closed-form component of the solution, which serves to accelerate the sampling process of MR diffusion models. Next, we analyze the sampling method currently used by MR Diffusion and demonstrate that this method corresponds to a variant of discretization for the reverse-time MRSDE.

#### 3.1 SOLUTIONS TO MEAN REVERTING SDES WITH NOISE PREDICTION

Ho et al. (2020) reported that score matching can be simplified to predicting noise, and Song et al. (2020b) revealed the connection between score function and noise prediction models, which is

$$\nabla_{\mathbf{x}_t} \log p(\mathbf{x}_t | \mathbf{x}_0) = -\frac{\epsilon_\theta(\mathbf{x}_t, \boldsymbol{\mu}, t)}{\sigma_t}, \quad (9)$$

where  $\sigma_t = \sigma_\infty \sqrt{1 - e^{-2 \int_0^t f(\tau) d\tau}}$  is the standard deviation of the transition distribution  $p(\mathbf{x}_t | \mathbf{x}_0)$ . Because  $\boldsymbol{\mu}$  is independent of  $t$  and  $\mathbf{x}$ , we substitute  $\epsilon_\theta(\mathbf{x}_t, \boldsymbol{\mu}, t)$  with  $\epsilon_\theta(\mathbf{x}_t, t)$  for notation simplicity. According to Eq.(9), we can rewrite Eq.(8) as

$$d\mathbf{x} = \left[ f(t)(\boldsymbol{\mu} - \mathbf{x}) + \frac{g^2(t)}{\sigma_t} \epsilon_\theta(\mathbf{x}_t, t) \right] dt + g(t)d\bar{w}. \quad (10)$$

Using Itô's formula (in the differential form), we can obtain the following semi-analytical solution:

**Proposition 1.** Given an initial value  $\mathbf{x}_s$  at time  $s \in [0, T]$ , the solution  $\mathbf{x}_t$  at time  $t \in [0, s]$  of Eq.(10) is

$$\mathbf{x}_t = \frac{\alpha_t}{\alpha_s} \mathbf{x}_s + \left(1 - \frac{\alpha_t}{\alpha_s}\right) \boldsymbol{\mu} + \alpha_t \int_s^t g^2(\tau) \frac{\epsilon_\theta(\mathbf{x}_\tau, \tau)}{\alpha_\tau \sigma_\tau} d\tau + \sqrt{- \int_s^t \frac{\alpha_t^2}{\alpha_\tau^2} g^2(\tau) d\tau} \mathbf{z}, \quad (11)$$

where we denote  $\alpha_t := e^{-\int_0^t f(\tau) d\tau}$  and  $\mathbf{z} \sim \mathcal{N}(\mathbf{0}, \mathbf{I})$ . The proof is in Appendix A.1.

However, the integral with respect to neural network output is still complicated. There have been several methods (Lu et al., 2022a; Zhang & Chen, 2022; Zhao et al., 2024) to estimate the integral numerically. We follow Lu et al. (2022b)'s method and introduce the half log-SNR  $\lambda_t := \log(\alpha_t/\sigma_t)$ . Since both  $f(t)$  and  $g(t)$  are deliberately designed to ensure that  $\alpha_t$  is monotonically decreasing over  $t$  and  $\sigma_t$  is monotonically increasing over  $t$ . Thus,  $\lambda_t$  is a strictly decreasing function of  $t$  and there exists an inverse function  $t(\lambda)$ . Then we can rewrite  $g(\tau)$  in Eq.(11) as

$$\begin{aligned} g^2(\tau) &= 2\sigma_\infty^2 f(\tau) = 2f(\tau)(\sigma_\tau^2 + \sigma_\infty^2 \alpha_\tau^2) = 2\sigma_\tau^2(f(\tau) + \frac{f(\tau)\sigma_\infty^2 \alpha_\tau^2}{\sigma_\tau^2}) \\ &= 2\sigma_\tau^2(f(\tau) + \frac{1}{2\sigma_\tau^2} \frac{d\sigma_\tau^2}{d\tau}) = -2\sigma_\tau^2 \frac{d\lambda_\tau}{d\tau}. \end{aligned} \quad (12)$$

By substituting Eq.(12) into Eq.(11), we obtain

$$\mathbf{x}_t = \frac{\alpha_t}{\alpha_s} \mathbf{x}_s + \left(1 - \frac{\alpha_t}{\alpha_s}\right) \boldsymbol{\mu} - 2\alpha_t \int_{\lambda_s}^{\lambda_t} e^{-\lambda} \boldsymbol{\epsilon}_\theta(\mathbf{x}_\lambda, \lambda) d\lambda + \sigma_t \sqrt{(e^{2(\lambda_t - \lambda_s)} - 1)} \mathbf{z}, \quad (13)$$

where  $\mathbf{x}_\lambda := \mathbf{x}_{t(\lambda)}$ ,  $\boldsymbol{\epsilon}_\theta(\mathbf{x}_\lambda, \lambda) := \boldsymbol{\epsilon}_\theta(\mathbf{x}_{t(\lambda)}, t(\lambda))$ . According to the methods of exponential integrators (Hochbruck & Ostermann, 2010; 2005), the  $(k-1)$ -th order Taylor expansion of  $\boldsymbol{\epsilon}_\theta(\mathbf{x}_\lambda, \lambda)$  and integration-by-parts of the integral part in Eq.(13) yields

$$-2\alpha_t \int_{\lambda_s}^{\lambda_t} e^{-\lambda} \boldsymbol{\epsilon}_\theta(\mathbf{x}_\lambda, \lambda) d\lambda = -2\sigma_t \sum_{n=0}^{k-1} \left[ \boldsymbol{\epsilon}_\theta^{(n)}(\mathbf{x}_{\lambda_s}, \lambda_s) \left( e^h - \sum_{m=0}^n \frac{(h)^m}{m!} \right) \right] + \mathcal{O}(h^{k+1}), \quad (14)$$

where  $h := \lambda_t - \lambda_s$ . We drop the discretization error term  $\mathcal{O}(h^{k+1})$  and estimate the derivatives with *backward difference method*. We name this algorithm as *MR Sampler-SDE-n-k*, where  $n$  means noise prediction and  $k$  is the order. We present details in Algorithm 1 and 2.

### 3.2 SOLUTIONS TO MEAN REVERTING ODES WITH NOISE PREDICTION

Song et al. (2020b) have illustrated that for any Itô SDE, there exists a *probability flow* ODE, sharing the same marginal distribution  $p_t(\mathbf{x})$  as a reverse-time SDE. Therefore, the solutions of PF-ODEs are also helpful in acceleration of sampling. Specifically, the PF-ODE corresponding to Eq.(10) is

$$\frac{d\mathbf{x}}{dt} = f(t) (\boldsymbol{\mu} - \mathbf{x}) + \frac{g^2(t)}{2\sigma_t} \boldsymbol{\epsilon}_\theta(\mathbf{x}_t, t). \quad (15)$$

The aforementioned equation exhibits a semi-linear structure with respect to  $\mathbf{x}$ , thus permitting resolution through the method of "variation of constants". We can draw the following conclusions:

**Proposition 2.** Given an initial value  $\mathbf{x}_s$  at time  $s \in [0, T]$ , the solution  $\mathbf{x}_t$  at time  $t \in [0, s]$  of Eq.(15) is

$$\mathbf{x}_t = \frac{\alpha_t}{\alpha_s} \mathbf{x}_s + \left(1 - \frac{\alpha_t}{\alpha_s}\right) \boldsymbol{\mu} + \alpha_t \int_s^t \frac{g^2(\tau)}{2\alpha_\tau \sigma_\tau} \boldsymbol{\epsilon}_\theta(\mathbf{x}_\tau, \tau) d\tau, \quad (16)$$

where  $\alpha_t := e^{-\int_0^t f(\tau) d\tau}$ . The proof is in Appendix A.1.

Then we follow the variable substitution and Eq.(12-14) in Section 3.1, and we obtain

$$\mathbf{x}_t = \frac{\alpha_t}{\alpha_s} \mathbf{x}_s + \left(1 - \frac{\alpha_t}{\alpha_s}\right) \boldsymbol{\mu} - \sigma_t \sum_{n=0}^{k-1} \left[ \boldsymbol{\epsilon}_\theta^{(n)}(\mathbf{x}_{\lambda_s}, \lambda_s) \left( e^h - \sum_{m=0}^n \frac{(h)^m}{m!} \right) \right] + \mathcal{O}(h^{k+1}), \quad (17)$$

where  $\boldsymbol{\epsilon}_\theta^{(n)}(\mathbf{x}_\lambda, \lambda) := \frac{d^n \boldsymbol{\epsilon}_\theta(\mathbf{x}_\lambda, \lambda)}{d\lambda^n}$  is the  $n$ -th order total derivatives of  $\boldsymbol{\epsilon}_\theta$  with respect to  $\lambda$ . By dropping the discretization error term  $\mathcal{O}(h^{k+1})$  and estimating the derivatives of  $\boldsymbol{\epsilon}_\theta(\mathbf{x}_{\lambda_s}, \lambda_s)$  with *backward difference method*, we design the sampling algorithm from the perspective of ODE (see Algorithm 3 and 4).

### 3.3 POSTERIOR SAMPLING FOR MEAN REVERTING DIFFUSION MODELS

In order to improve the sampling process of Mean Reverting Diffusion, Luo et al. (2024b) proposed the *posterior sampling* algorithm. They define a monotonically increasing time series  $\{t_i\}_{i=0}^T$  and

270 the reverse process as a Markov chain:  
 271

$$272 \quad p(\mathbf{x}_{1:T} | \mathbf{x}_0) = p(\mathbf{x}_T | \mathbf{x}_0) \prod_{i=2}^T p(\mathbf{x}_{i-1} | \mathbf{x}_i, \mathbf{x}_0) \text{ and } \mathbf{x}_T \sim \mathcal{N}(\mathbf{0}, \mathbf{I}), \quad (18)$$

275 where we denote  $\mathbf{x}_i := \mathbf{x}_{t_i}$  for simplicity. They obtain an optimal posterior distribution by mini-  
 276 mizing the negative log-likelihood, which is a Gaussian distribution given by  
 277

$$\begin{aligned} 278 \quad p(\mathbf{x}_{i-1} | \mathbf{x}_i, \mathbf{x}_0) &= \mathcal{N}(\mathbf{x}_{i-1} | \tilde{\boldsymbol{\mu}}_i(\mathbf{x}_i, \mathbf{x}_0), \tilde{\beta}_i \mathbf{I}), \\ 279 \quad \tilde{\boldsymbol{\mu}}_i(\mathbf{x}_i, \mathbf{x}_0) &= \frac{(1 - \alpha_{i-1}^2)\alpha_i}{(1 - \alpha_i^2)\alpha_{i-1}}(\mathbf{x}_i - \boldsymbol{\mu}) + \frac{1 - \frac{\alpha_i^2}{\alpha_{i-1}^2}}{1 - \alpha_i^2}\alpha_{i-1}(\mathbf{x}_0 - \boldsymbol{\mu}) + \boldsymbol{\mu}, \\ 280 \quad \tilde{\beta}_i &= \frac{(1 - \alpha_{i-1}^2)(1 - \frac{\alpha_i^2}{\alpha_{i-1}^2})}{1 - \alpha_i^2}, \end{aligned} \quad (19)$$

285 where  $\alpha_i = e^{-\int_0^i f(\tau)d\tau}$  and  $\mathbf{x}_0 = (\mathbf{x}_i - \boldsymbol{\mu} - \sigma_i \boldsymbol{\epsilon}_\theta(\mathbf{x}_i, \boldsymbol{\mu}, t_i)) / \alpha_i + \boldsymbol{\mu}$ . Actually, the repara-  
 286 meterization of posterior distribution in Eq.(19) is equivalent to a variant of the Euler-Maruyama dis-  
 287 cretization of the reverse-time SDE (see details in Appendix A.2). Specifically, the Euler-Maruyama  
 288 method computes the solution in the following form:  
 289

$$290 \quad \mathbf{x}_t = \mathbf{x}_s + \int_s^t \left[ f(\tau) (\boldsymbol{\mu} - \mathbf{x}_\tau) + \frac{g^2(\tau)}{\sigma_\tau} \boldsymbol{\epsilon}_\theta(\mathbf{x}_\tau, \tau) \right] d\tau + \int_s^t g(\tau) d\bar{\mathbf{w}}_\tau, \quad (20)$$

292 which introduces approximation errors from both the analytical term and the non-linear component  
 293 associated with neural network predictions. In contrast, our approach delivers an exact solution for  
 294 the analytical part, leading to reduced approximation errors and a higher order of convergence.  
 295

## 296 4 FAST SAMPLERS FOR MEAN REVERTING DIFFUSION WITH DATA 297 PREDICTION

300 Unfortunately, the sampler based on noise prediction can exhibit substantial instability, particularly  
 301 with small NFEs, and may perform even worse than *posterior sampling*. It is well recognized that  
 302 the Taylor expansion has a limited convergence domain, primarily influenced by the derivatives of  
 303 the neural networks. In fact, higher-order derivatives often result in smaller convergence radii. Dur-  
 304 ing the training phase, the noise prediction neural network is designed to fit normally distributed  
 305 Gaussian noise. When the standard deviation of this Gaussian noise is set to 1, the values of sam-  
 306 ples can fall outside the range of  $[-1, 1]$  with a probability of 34.74%. This discrepancy results  
 307 in numerical instability in the output of the neural network, causing its derivatives to exhibit more  
 308 pronounced fluctuations (refer to the experimental results in Section 5 for further details). Conse-  
 309 quently, the numerical instability leads to very narrow convergence domains, or in extreme cases, no  
 310 convergence at all, which ultimately yields awful sampling results.

311 Lu et al. (2022b) have identified that the choice of parameterization for either ODEs or SDEs is  
 312 critical for the boundedness of the convergent solution. In contrast to noise prediction, the data  
 313 prediction model (Salimans & Ho, 2022) focuses on fitting  $\mathbf{x}_0$ , ensuring that its output remains  
 314 strictly confined within the bounds of  $[-1, 1]$ , thereby achieving high numerical stability.

### 315 4.1 SOLUTIONS TO MEAN REVERTING SDEs WITH DATA PREDICTION

316 According to Eq.(7), we can parameterize  $\mathbf{x}_0$  as follows:

$$317 \quad \boldsymbol{\epsilon}_\theta(\mathbf{x}_t, t) = \frac{\mathbf{x}_t - \alpha_t \mathbf{x}_\theta(\mathbf{x}_t, t) - (1 - \alpha_t) \boldsymbol{\mu}}{\sigma_t}. \quad (21)$$

318 By substituting Eq.(21) into Eq.(10), we derive the following SDE that incorporates data prediction:  
 319

$$320 \quad d\mathbf{x} = \left( \frac{g^2(t)}{\sigma_t^2} - f(t) \right) \mathbf{x} + \left[ f(t) - \frac{g^2(t)}{\sigma_t^2} (1 - \alpha_t) \right] \boldsymbol{\mu} - \frac{g^2(t)}{\sigma_t^2} \alpha_t \mathbf{x}_\theta(\mathbf{x}_t, t) + g(t) d\bar{\mathbf{w}}. \quad (22)$$

This equation remains semi-linear with respect to  $\mathbf{x}$  and thus we can employ Itô's formula (in the differential form) to obtain the solution to Eq.(22).

**Proposition 3.** Given an initial value  $\mathbf{x}_s$  at time  $s \in [0, T]$ , the solution  $\mathbf{x}_t$  at time  $t \in [0, s]$  of Eq.(22) is

$$\begin{aligned} \mathbf{x}_t &= \frac{\sigma_t}{\sigma_s} e^{-(\lambda_t - \lambda_s)} \mathbf{x}_s + \boldsymbol{\mu} \left( 1 - \frac{\alpha_t}{\alpha_s} e^{-2(\lambda_t - \lambda_s)} - \alpha_t + \alpha_t e^{-2(\lambda_t - \lambda_s)} \right) \\ &\quad + 2\alpha_t \int_{\lambda_s}^{\lambda_t} e^{-2(\lambda_t - \lambda)} \mathbf{x}_\theta(\mathbf{x}_\lambda, \lambda) d\lambda + \sigma_t \sqrt{1 - e^{-2(\lambda_t - \lambda_s)}} \mathbf{z}, \end{aligned} \quad (23)$$

where  $\mathbf{z} \sim \mathcal{N}(\mathbf{0}, \mathbf{I})$ . The proof is in Appendix A.1.

Then we apply Taylor expansion and integration-by-parts to estimate the integral part in Eq.(23) and obtain the stochastic sampling algorithm for data prediction (see details in Algorithm 5 and 6).

## 4.2 SOLUTIONS TO MEAN REVERTING ODES WITH DATA PREDICTION

By substituting Eq.(21) into Eq.(15), we can obtain the following ODE parameterized by data prediction.

$$\frac{d\mathbf{x}}{dt} = \left( \frac{g^2(t)}{2\sigma_t^2} - f(t) \right) \mathbf{x} + \left[ f(t) - \frac{g^2(t)}{2\sigma_t^2} (1 - \alpha_t) \right] \boldsymbol{\mu} - \frac{g^2(t)}{2\sigma_t^2} \alpha_t \mathbf{x}_\theta(\mathbf{x}_t, t). \quad (24)$$

The incorporation of the parameter  $\boldsymbol{\mu}$  does not disrupt the semi-linear structure of the equation with respect to  $\mathbf{x}$ , and  $\boldsymbol{\mu}$  is not coupled to the neural network. This implies that analytical part of solutions can still be derived concerning both  $\mathbf{x}$  and  $\boldsymbol{\mu}$ . We present the solution below (see Appendix A.1 for a detailed derivation).

**Proposition 4.** Given an initial value  $\mathbf{x}_s$  at time  $s \in [0, T]$ , the solution  $\mathbf{x}_t$  at time  $t \in [0, s]$  of Eq.(24) is

$$\mathbf{x}_t = \frac{\sigma_t}{\sigma_s} \mathbf{x}_s + \boldsymbol{\mu} \left( 1 - \frac{\sigma_t}{\sigma_s} + \frac{\sigma_t}{\sigma_s} \alpha_s - \alpha_t \right) + \sigma_t \int_{\lambda_s}^{\lambda_t} e^\lambda \mathbf{x}_\theta(\mathbf{x}_\lambda, \lambda) d\lambda. \quad (25)$$

Similarly, only the neural network component requires approximation through the exponential integrator method (Hochbruck & Ostermann, 2005; 2010). And we can obtain the deterministic sampling algorithm for data prediction (see Algorithm 7 and 8 for details).

## 4.3 TRANSFORMATION BETWEEN THREE KINDS OF PARAMETERIZATIONS

There are three mainstream parameterization methods. Ho et al. (2020) introduced a training objective based on noise prediction, while Salimans & Ho (2022) proposed parameterization strategies for data and velocity prediction to keep network outputs stable under the variation of time or log-SNR. All three methods can be regarded as score matching approaches (Song et al., 2020b; Hyvärinen & Dayan, 2005) with weighted coefficients. To ensure our proposed algorithm is compatible with these parameterization strategies, it is necessary to provide transformation formulas for each pairs among the three strategies.

The transformation formula between noise prediction and data prediction can be easily derived from Eq.(7):

$$\begin{cases} \mathbf{x}_\theta(t) = \frac{\mathbf{x}_t - (1 - \alpha_t)\boldsymbol{\mu} - \sigma_t \boldsymbol{\epsilon}_\theta(t)}{\alpha_t}, \\ \boldsymbol{\epsilon}_\theta(t) = \frac{\mathbf{x}_t - \alpha_t \mathbf{x}_\theta(t) - (1 - \alpha_t)\boldsymbol{\mu}}{\sigma_t}. \end{cases} \quad (26)$$

For velocity prediction, we define  $\phi_t := \arctan(\frac{\sigma_t}{\sigma_\infty \alpha_t})$ , which is slightly different from the definition of Salimans & Ho (2022). Then we have  $\alpha_t = \cos \phi_t$ ,  $\sigma_t = \sigma_\infty \sin \phi_t$  and hence  $\mathbf{x}_t = \mathbf{x}_0 \cos \phi_t + \boldsymbol{\mu}(1 - \cos \phi_t) + \sigma_\infty \sin(\phi_t) \boldsymbol{\epsilon}$ . And the definition of  $\mathbf{v}(t)$  is

$$\mathbf{v}_t = \frac{d\mathbf{x}_t}{d\phi_t} = \boldsymbol{\mu} \sin \phi_t - \mathbf{x}_0 \sin \phi_t + \sigma_\infty \cos(\phi_t) \boldsymbol{\epsilon}. \quad (27)$$

If we have a score function model  $\mathbf{v}_\theta(t)$  trained with velocity prediction, we can obtain  $\mathbf{x}_\theta(t)$  and  $\boldsymbol{\epsilon}_\theta(t)$  by (see Appendix A.3 for detailed derivations)

$$\mathbf{x}_\theta(t) = \mathbf{x}_t \cos \phi_t + \boldsymbol{\mu}(1 - \cos \phi_t) - \mathbf{v}_\theta(t) \sin \phi_t, \quad (28)$$

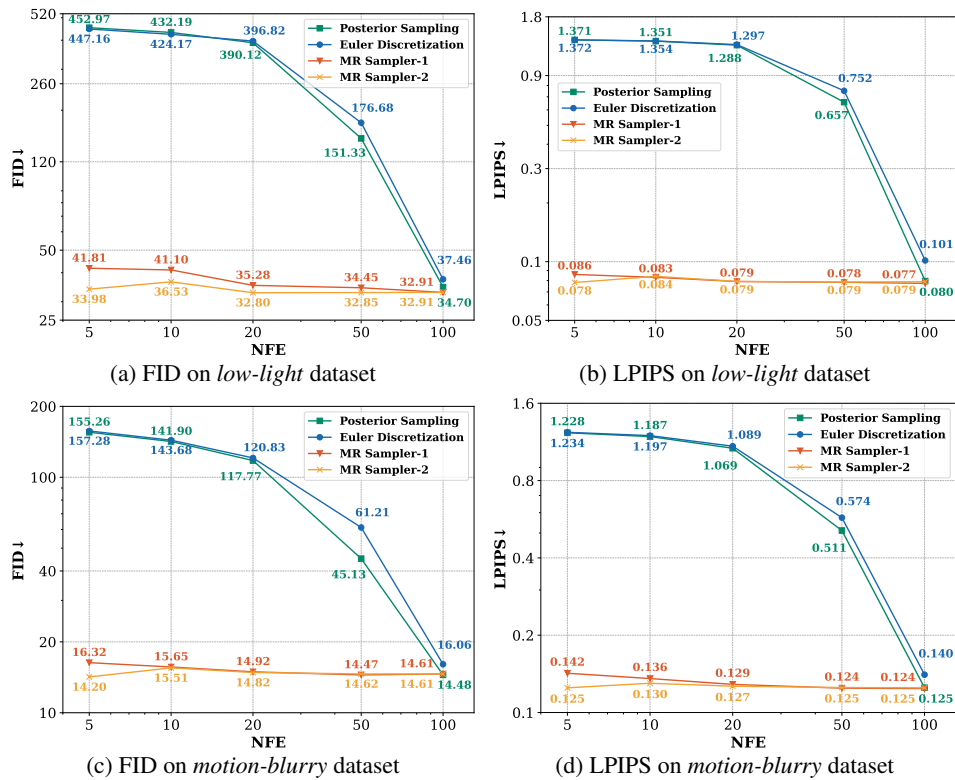
$$\boldsymbol{\epsilon}_\theta(t) = (\mathbf{v}_\theta(t) \cos \phi_t + \mathbf{x}_t \sin \phi_t - \boldsymbol{\mu} \sin \phi_t) / \sigma_\infty. \quad (29)$$

378    **5 EXPERIMENTS**  
 379  
 380

381    In this section, we conduct extensive experiments to show that MR Sampler can significantly speed  
 382    up the sampling of existing MR Diffusion. To rigorously validate the effectiveness of our method,  
 383    we follow the settings and checkpoints from Luo et al. (2024a) and only modify the sampling part.  
 384    Our experiment is divided into three parts. Section 5.1 compares the sampling results for different  
 385    NFE cases. Section 5.2 studies the effects of different parameter settings on our algorithm, including  
 386    network parameterizations and solver types. In Section 5.3, we visualize the sampling trajectories to  
 387    show the speedup achieved by MR Sampler and analyze why noise prediction gets obviously worse  
 388    when NFE is less than 20.

389  
 390    **5.1 MAIN RESULTS**  
 391

392    Following Luo et al. (2024a), we conduct experiments with ten different types of image degradation:  
 393    blurry, hazy, JPEG-compression, low-light, noisy, raindrop, rainy, shadowed, snowy, and inpainting  
 394    (see Appendix D.1 for details). We adopt LPIPS (Zhang et al., 2018) and FID (Heusel et al., 2017)  
 395    as main metrics for perceptual evaluation, and also report PSNR and SSIM (Wang et al., 2004) for  
 396    reference. We compare MR Sampler with other sampling methods, including posterior sampling  
 397    (Luo et al., 2024b) and Euler-Maruyama discretization (Kloeden et al., 1992). We take two tasks  
 398    as examples and the metrics are shown in Figure 2. Unless explicitly mentioned, we always use  
 399    MR Sampler based on SDE solver, with data prediction and uniform  $\lambda$ . The complete experimental  
 400    results can be found in Appendix D.3. The results demonstrate that MR Sampler converges in a few  
 401    (5 or 10) steps and produces samples with stable quality. Our algorithm significantly reduces the  
 402    time cost without compromising sampling performance, which is of great practical value for MR  
 403    Diffusion.



426    Figure 2: **Perceptual evaluations on *low-light* and *motion-blurry* datasets.**  
 427  
 428  
 429

432    5.2 EFFECTS OF PARAMETER CHOICE  
 433

434    In Table 2, we compare the results of two network parameterizations. The data prediction shows  
 435    stable performance across different NFEs. The noise prediction performs similarly to data prediction  
 436    with large NFEs, but its performance deteriorates significantly with smaller NFEs. The detailed  
 437    analysis can be found in Section 5.3. In Table 3, we compare MR Sampler-ODE-d-2 and MR  
 438    Sampler-SDE-d-2 on the *inpainting* task, which are derived from PF-ODE and reverse-time SDE  
 439    respectively. SDE-based solver works better with a large NFE, whereas ODE-based solver is more  
 440    effective with a small NFE. In general, neither solver type is inherently better.

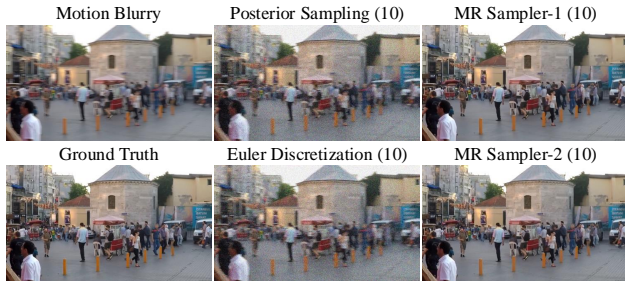
441    Table 2: Ablation study of network parameteriza-  
 442    tions on the Rain100H dataset.

NFE	Parameterization	LPIPS↓	FID↓	PSNR↑	SSIM↑
50	Noise Prediction	<b>0.0606</b>	<b>27.28</b>	<b>28.89</b>	<b>0.8615</b>
	Data Prediction	0.0620	27.65	28.85	0.8602
20	Noise Prediction	0.1429	47.31	27.68	0.7954
	Data Prediction	<b>0.0635</b>	<b>27.79</b>	<b>28.60</b>	<b>0.8559</b>
10	Noise Prediction	1.376	402.3	6.623	0.0114
	Data Prediction	<b>0.0678</b>	<b>29.54</b>	<b>28.09</b>	<b>0.8483</b>
5	Noise Prediction	1.416	447.0	5.755	0.0051
	Data Prediction	<b>0.0637</b>	<b>26.92</b>	<b>28.82</b>	<b>0.8685</b>

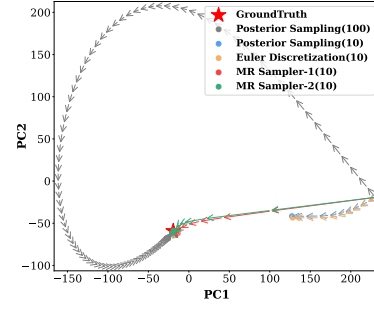
441    Table 3: Ablation study of solver types on the  
 442    CelebA-HQ dataset.

NFE	Solver Type	LPIPS↓	FID↓	PSNR↑	SSIM↑
50	ODE	0.0499	22.91	28.49	0.8921
	SDE	<b>0.0402</b>	<b>19.09</b>	<b>29.15</b>	<b>0.9046</b>
20	ODE	0.0475	21.35	28.51	0.8940
	SDE	<b>0.0408</b>	<b>19.13</b>	<b>28.98</b>	<b>0.9032</b>
10	ODE	<b>0.0417</b>	19.44	<b>28.94</b>	<b>0.9048</b>
	SDE	0.0437	<b>19.29</b>	28.48	0.8996
5	ODE	<b>0.0526</b>	27.44	<b>31.02</b>	<b>0.9335</b>
	SDE	0.0529	<b>24.02</b>	28.35	0.8930

452  
 453    5.3 ANALYSIS  
 454



467    (a) Sampling results.



467    (b) Trajectory.

468    Figure 3: **Sampling trajectories.** In (a), we compare our method (with order 1 and order 2) and  
 469    previous sampling methods (i.e., posterior sampling and Euler discretization) on a motion blurry im-  
 470    age. The numbers in parentheses indicate the NFE. In (b), we illustrate trajectories of each sampling  
 471    method. Previous methods need to take many unnecessary paths to converge. With few NFE, they  
 472    fail to reach the ground truth (i.e., the location of  $x_0$ ). Our methods follow a more direct trajectory.  
 473

474    **Sampling trajectory.** Inspired by the design idea of NCSN (Song & Ermon, 2019), we provide  
 475    a new perspective of diffusion sampling process. Song & Ermon (2019) consider each data point  
 476    (e.g., an image) as a point in high-dimensional space. During the diffusion process, noise is added  
 477    to each point  $x_0$ , causing it to spread throughout the space, while the score function (a neural net-  
 478    work) *remembers* the direction towards  $x_0$ . In the sampling process, we start from a random point  
 479    by sampling a Gaussian distribution and follow the guidance of the reverse-time SDE (or PF-ODE)  
 480    and the score function to locate  $x_0$ . By connecting each intermediate state  $x_t$ , we obtain a sam-  
 481    pling trajectory. However, this trajectory exists in a high-dimensional space, making it difficult to  
 482    visualize. Therefore, we use Principal Component Analysis (PCA) to reduce  $x_t$  to two dimensions,  
 483    obtaining the projection of the sampling trajectory in 2D space. As shown in Figure 3, we present  
 484    an example. Previous sampling methods (Luo et al., 2024b) often require a long path to find  $x_0$ ,  
 485    and reducing NFE can lead to cumulative errors, making it impossible to locate  $x_0$ . In contrast, our  
 algorithm produces more direct trajectories, allowing us to find  $x_0$  with fewer NFEs.

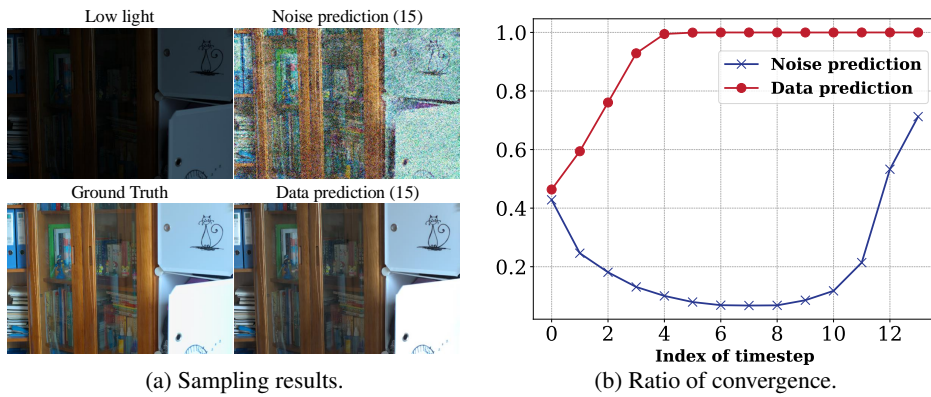


Figure 4: **Convergence of noise prediction and data prediction.** In (a), we choose a low-light image for example. The numbers in parentheses indicate the NFE. In (b), we illustrate the ratio of components of neural network output that satisfy the Taylor expansion convergence requirement.

**Numerical stability of parameterizations.** From Table 1, we observe poor sampling results for noise prediction in the case of few NFEs. The reason may be that the neural network parameterized by noise prediction is numerically unstable. Recall that we used Taylor expansion in Eq.(14), and the condition for the equality to hold is  $|\lambda - \lambda_s| < R(s)$ . And the radius of convergence  $R(t)$  can be calculated by

$$\frac{1}{R(t)} = \lim_{n \rightarrow \infty} \left| \frac{c_{n+1}(t)}{c_n(t)} \right|, \quad (30)$$

where  $c_n(t)$  is the coefficient of the  $n$ -th term in Taylor expansion. We are unable to compute this limit and can only compute the  $n = 1$  case as an approximation. The output of the neural network can be viewed as a vector, with each component corresponding to a radius of convergence. At each time step, we count the ratio of components that satisfy  $R_i(s) > |\lambda - \lambda_s|$  as a criterion for judging the convergence, where  $i$  denotes the  $i$ -th component. As shown in Figure 4, the neural network parameterized by data prediction meets the convergence criteria at almost every step. However, the neural network parameterized by noise prediction always has components that cannot converge, which will lead to large errors and failed sampling. Therefore, data prediction has better numerical stability and is a more recommended choice.

## 6 CONCLUSION

We have developed a the fast sampling algorithm of MR Diffusion. Compared with DPMs, MR Diffusion is different in SDE and thus not adaptable to existing training-free fast samplers. We propose MR Sampler for acceleration of sampling of MR Diffusion. We solve the reverse-time SDE and PF-ODE derived from MRSDE and find a semi-analytical solution. We adopt the methods of *exponential integrators* to estimate the non-linear integral part. Abundant experiments demonstrate that our algorithm achieves small errors and fast convergence. Additionally, we visualize sampling trajectories and explain why the parameterization of noise prediction does not perform well in the case of small NFEs.

**Limitations and broader impact.** Despite the effectiveness of MR Sampler, our method is still inferior to distillation methods (Song et al., 2023; Luo et al., 2023a) within less than 5 NFEs. Additionally, our method can only accelerate sampling, but cannot improve the upper limit of sampling quality.

## REPRODUCIBILITY STATEMENT

Our codes are based on the official code of MR Diffusion (Luo et al., 2023b) and DPM-Solver (Lu et al., 2022b). And we use the checkpoints and datasets provided by MR Diffusion (Luo et al., 2023b). We will release them after the blind review.

540 REFERENCES  
541

- 542 Eirikur Agustsson and Radu Timofte. Ntire 2017 challenge on single image super-resolution: dataset  
543 and study. In *Proceedings of the IEEE Conference on Computer Vision and Pattern Recognition*  
544 (*CVPR*) Workshops, pp. 126–135, 2017.
- 545 Brian DO Anderson. Reverse-time diffusion equation models. *Stochastic Processes and their Ap-*  
546 *plications*, 12(3):313–326, 1982.  
547
- 548 Hyungjin Chung, Byeongsu Sim, and Jong Chul Ye. Come-closer-diffuse-faster: Accelerating con-  
549 ditional diffusion models for inverse problems through stochastic contraction. In *Proceedings of*  
550 *the IEEE/CVF Conference on Computer Vision and Pattern Recognition*, pp. 12413–12422, 2022.
- 551 Prafulla Dhariwal and Alexander Nichol. Diffusion models beat gans on image synthesis. *Advances*  
552 *in neural information processing systems*, 34:8780–8794, 2021.  
553
- 554 Martin Heusel, Hubert Ramsauer, Thomas Unterthiner, Bernhard Nessler, and Sepp Hochreiter.  
555 Gans trained by a two time-scale update rule converge to a local nash equilibrium. *Advances in*  
556 *neural information processing systems*, 30, 2017.  
557
- 558 Jonathan Ho and Tim Salimans. Classifier-free diffusion guidance. *arXiv preprint*  
559 *arXiv:2207.12598*, 2022.  
560
- 561 Jonathan Ho, Ajay Jain, and Pieter Abbeel. Denoising diffusion probabilistic models. *Advances in*  
562 *neural information processing systems*, 33:6840–6851, 2020.  
563
- 564 Jonathan Ho, William Chan, Chitwan Saharia, Jay Whang, Ruiqi Gao, Alexey Gritsenko, Diederik P  
565 Kingma, Ben Poole, Mohammad Norouzi, David J Fleet, et al. Imagen video: High definition  
566 video generation with diffusion models. *arXiv preprint arXiv:2210.02303*, 2022a.  
567
- 568 Jonathan Ho, Tim Salimans, Alexey Gritsenko, William Chan, Mohammad Norouzi, and David J  
569 Fleet. Video diffusion models. *Advances in Neural Information Processing Systems*, 35:8633–  
8646, 2022b.  
570
- 571 Marlis Hochbruck and Alexander Ostermann. Explicit exponential runge–kutta methods for semi-  
572 linear parabolic problems. *SIAM Journal on Numerical Analysis*, 43(3):1069–1090, 2005.  
573
- 574 Marlis Hochbruck and Alexander Ostermann. Exponential integrators. *Acta Numerica*, 19:209–286,  
2010.  
575
- 576 Aapo Hyvärinen and Peter Dayan. Estimation of non-normalized statistical models by score match-  
577 ing. *Journal of Machine Learning Research*, 6(4), 2005.  
578
- 579 Tero Karras. Progressive growing of gans for improved quality, stability, and variation. *arXiv*  
*preprint arXiv:1710.10196*, 2017.  
580
- 581 Tero Karras, Miika Aittala, Timo Aila, and Samuli Laine. Elucidating the design space of diffusion-  
582 based generative models. *Advances in neural information processing systems*, 35:26565–26577,  
2022.  
583
- 584 Peter E Kloeden, Eckhard Platen, Peter E Kloeden, and Eckhard Platen. *Stochastic differential*  
585 *equations*. Springer, 1992.  
586
- 587 Luping Liu, Yi Ren, Zhijie Lin, and Zhou Zhao. Pseudo numerical methods for diffusion models on  
588 manifolds. *arXiv preprint arXiv:2202.09778*, 2022a.  
589
- 590 Xingchao Liu, Chengyue Gong, and Qiang Liu. Flow straight and fast: Learning to generate and  
591 transfer data with rectified flow. *arXiv preprint arXiv:2209.03003*, 2022b.  
592
- 593 Yun-Fu Liu, Da-Wei Jaw, Shih-Chia Huang, and Jenq-Neng Hwang. Desnownet: Context-aware  
deep network for snow removal. *IEEE Transactions on Image Processing*, 27(6):3064–3073,  
2018.

- 594 Cheng Lu, Yuhao Zhou, Fan Bao, Jianfei Chen, Chongxuan Li, and Jun Zhu. Dpm-solver: A fast  
 595 ode solver for diffusion probabilistic model sampling in around 10 steps. *Advances in Neural*  
 596 *Information Processing Systems*, 35:5775–5787, 2022a.
- 597 Cheng Lu, Yuhao Zhou, Fan Bao, Jianfei Chen, Chongxuan Li, and Jun Zhu. Dpm-solver++: Fast  
 598 solver for guided sampling of diffusion probabilistic models. *arXiv preprint arXiv:2211.01095*,  
 599 2022b.
- 600 Andreas Lugmayr, Martin Danelljan, Andres Romero, Fisher Yu, Radu Timofte, and Luc Van Gool.  
 601 Repaint: Inpainting using denoising diffusion probabilistic models. In *Proceedings of the*  
 602 *IEEE/CVF Conference on Computer Vision and Pattern Recognition*, pp. 11461–11471, 2022.
- 603 Simian Luo, Yiqin Tan, Longbo Huang, Jian Li, and Hang Zhao. Latent consistency models: Synthe-  
 604 sizing high-resolution images with few-step inference. *arXiv preprint arXiv:2310.04378*, 2023a.
- 605 Ziwei Luo, Fredrik K Gustafsson, Zheng Zhao, Jens Sjölund, and Thomas B Schön. Image restora-  
 606 tion with mean-reverting stochastic differential equations. *arXiv preprint arXiv:2301.11699*,  
 607 2023b.
- 608 Ziwei Luo, Fredrik K Gustafsson, Zheng Zhao, Jens Sjölund, and Thomas B Schön. Refusion:  
 609 Enabling large-size realistic image restoration with latent-space diffusion models. In *Proceedings*  
 610 *of the IEEE/CVF conference on computer vision and pattern recognition*, pp. 1680–1691, 2023c.
- 611 Ziwei Luo, Fredrik K Gustafsson, Zheng Zhao, Jens Sjölund, and Thomas B Schön. Controlling  
 612 vision-language models for multi-task image restoration. In *The Twelfth International Conference*  
 613 *on Learning Representations*, 2024a.
- 614 Ziwei Luo, Fredrik K Gustafsson, Zheng Zhao, Jens Sjölund, and Thomas B Schön. Photo-realistic  
 615 image restoration in the wild with controlled vision-language models. In *Proceedings of the*  
 616 *IEEE/CVF Conference on Computer Vision and Pattern Recognition*, pp. 6641–6651, 2024b.
- 617 David Martin, Charless Fowlkes, Doron Tal, and Jitendra Malik. A database of human segmented  
 618 natural images and its application to evaluating segmentation algorithms and measuring ecological  
 619 statistics. In *Proceedings of the 18th IEEE International Conference on Computer Vision (ICCV)*,  
 620 volume 2, pp. 416–423. IEEE, 2001.
- 621 Seungjun Nah, Tae Hyun Kim, and Kyoung Mu Lee. Deep multi-scale convolutional neural network  
 622 for dynamic scene deblurring. In *Proceedings of the IEEE Conference on Computer Vision and*  
 623 *Pattern Recognition (CVPR)*, pp. 3883–3891, 2017.
- 624 Rui Qian, Robby T Tan, Wenhan Yang, Jiajun Su, and Jiaying Liu. Attentive generative adversarial  
 625 network for raindrop removal from a single image. In *Proceedings of the IEEE Conference on*  
 626 *Computer Vision and Pattern Recognition*, pp. 2482–2491, 2018.
- 627 Xu Qin, Zhilin Wang, Yuanchao Bai, Xiaodong Xie, and Huizhu Jia. FFA-Net: Feature fusion  
 628 attention network for single image dehazing. In *Proceedings of the AAAI Conference on Artificial*  
 629 *Intelligence*, pp. 11908–11915, 2020a.
- 630 Xu Qin, Zhilin Wang, Yuanchao Bai, Xiaodong Xie, and Huizhu Jia. Ffa-net: Feature fusion at-  
 631 tention network for single image dehazing. In *Proceedings of the AAAI conference on artificial*  
 632 *intelligence*, volume 34, pp. 11908–11915, 2020b.
- 633 Liangqiong Qu, Jiandong Tian, Shengfeng He, Yandong Tang, and Rynson WH Lau. Deshadownet:  
 634 A multi-context embedding deep network for shadow removal. In *Proceedings of the IEEE Con-*  
 635 *ference on Computer Vision and Pattern Recognition*, pp. 4067–4075, 2017.
- 636 Robin Rombach, Andreas Blattmann, Dominik Lorenz, Patrick Esser, and Björn Ommer. High-  
 637 resolution image synthesis with latent diffusion models. In *Proceedings of the IEEE/CVF confer-*  
 638 *ence on computer vision and pattern recognition*, pp. 10684–10695, 2022.
- 639 Nataniel Ruiz, Yuanzhen Li, Varun Jampani, Yael Pritch, Michael Rubinstein, and Kfir Aberman.  
 640 Dreambooth: Fine tuning text-to-image diffusion models for subject-driven generation. In *Pro-*  
 641 *ceedings of the IEEE/CVF conference on computer vision and pattern recognition*, pp. 22500–  
 642 22510, 2023.

- 648 Tim Salimans and Jonathan Ho. Progressive distillation for fast sampling of diffusion models. *arXiv  
649 preprint arXiv:2202.00512*, 2022.  
650
- 651 Simo Särkkä and Arno Solin. *Applied stochastic differential equations*, volume 10. Cambridge  
652 University Press, 2019.
- 653 H Sheikh. Live image quality assessment database release 2. <http://live.ece.utexas.edu/research/quality>, 2005.  
654
- 655 Jiaming Song, Chenlin Meng, and Stefano Ermon. Denoising diffusion implicit models. *arXiv  
656 preprint arXiv:2010.02502*, 2020a.  
657
- 658 Yang Song and Stefano Ermon. Generative modeling by estimating gradients of the data distribution.  
659 *Advances in neural information processing systems*, 32, 2019.  
660
- 661 Yang Song and Stefano Ermon. Improved techniques for training score-based generative models.  
662 *Advances in neural information processing systems*, 33:12438–12448, 2020.  
663
- 664 Yang Song, Jascha Sohl-Dickstein, Diederik P Kingma, Abhishek Kumar, Stefano Ermon, and Ben  
665 Poole. Score-based generative modeling through stochastic differential equations. *arXiv preprint  
arXiv:2011.13456*, 2020b.  
666
- 667 Yang Song, Conor Durkan, Iain Murray, and Stefano Ermon. Maximum likelihood training of  
668 score-based diffusion models. *Advances in neural information processing systems*, 34:1415–  
669 1428, 2021.  
670
- 671 Yang Song, Prafulla Dhariwal, Mark Chen, and Ilya Sutskever. Consistency models. *arXiv preprint  
arXiv:2303.01469*, 2023.  
672
- 673 Radu Timofte, Eirikur Agustsson, Luc Van Gool, Ming-Hsuan Yang, and Lei Zhang. NTIRE 2017  
674 challenge on single image super-resolution: methods and results. In *Proceedings of the IEEE  
Conference on Computer Vision and Pattern Recognition (CVPR) Workshops*, pp. 114–125, 2017.  
675
- 676 Zhou Wang, Alan C Bovik, Hamid R Sheikh, and Eero P Simoncelli. Image quality assessment:  
677 from error visibility to structural similarity. *IEEE transactions on image processing*, 13(4):600–  
678 612, 2004.  
679
- 680 Chen Wei, Wenjing Wang, Wenhan Yang, and Jiaying Liu. Deep retinex decomposition for low-light  
681 enhancement. *arXiv preprint arXiv:1808.04560*, 2018.  
682
- 683 Wenhao Yang, Robby T Tan, Jiashi Feng, Jiaying Liu, Zongming Guo, and Shuicheng Yan. Deep  
684 joint rain detection and removal from a single image. In *Proceedings of the IEEE conference on  
computer vision and pattern recognition*, pp. 1357–1366, 2017.  
685
- 686 Hu Ye, Jun Zhang, Sibo Liu, Xiao Han, and Wei Yang. Ip-adapter: Text compatible image prompt  
687 adapter for text-to-image diffusion models. *arXiv preprint arXiv:2308.06721*, 2023.  
688
- 689 Lvmian Zhang, Anyi Rao, and Maneesh Agrawala. Adding conditional control to text-to-image  
690 diffusion models. In *Proceedings of the IEEE/CVF International Conference on Computer Vision*,  
691 pp. 3836–3847, 2023.  
692
- 693 Qinsheng Zhang and Yongxin Chen. Fast sampling of diffusion models with exponential integrator.  
694 *arXiv preprint arXiv:2204.13902*, 2022.  
695
- 696 Richard Zhang, Phillip Isola, Alexei A Efros, Eli Shechtman, and Oliver Wang. The unreasonable  
697 effectiveness of deep features as a perceptual metric. In *Proceedings of the IEEE conference on  
computer vision and pattern recognition*, pp. 586–595, 2018.  
698
- 699 Wenliang Zhao, Lujia Bai, Yongming Rao, Jie Zhou, and Jiwen Lu. Unipc: A unified predictor-  
700 corrector framework for fast sampling of diffusion models. *Advances in Neural Information  
701 Processing Systems*, 36, 2024.  
702
- Zhenyu Zhou, Defang Chen, Can Wang, and Chun Chen. Fast ode-based sampling for diffusion  
models in around 5 steps. In *Proceedings of the IEEE/CVF Conference on Computer Vision and  
Pattern Recognition*, pp. 7777–7786, 2024.

702 APPENDIX  
 703

704 We include several appendices with derivations, additional details and results. In Appendix A, we  
 705 provide derivations of propositions in Section 3 and 4, equivalence between *posterior sampling* and  
 706 Euler-Maruyama discretization, and velocity prediction, respectively. In Appendix B, we compare  
 707 the notations used in this paper and MRSDE (Luo et al., 2023b). In Appendix C, we list detailed  
 708 algorithms of MR Sampler with various orders and parameterizations. In Appendix D, we present  
 709 details about datasets, settings and results in experiments. In Appendix E, we provide an in-depth  
 710 discussion on determining the optimal NFE.

711  
 712 A DERIVATION DETAILS  
 713

714 A.1 PROOFS OF PROPOSITIONS  
 715

716 **Proposition 1.** Given an initial value  $\mathbf{x}_s$  at time  $s \in [0, T]$ , the solution  $\mathbf{x}_t$  at time  $t \in [0, s]$  of  
 717 Eq.(10) is

$$718 \quad \mathbf{x}_t = \frac{\alpha_t}{\alpha_s} \mathbf{x}_s + \left(1 - \frac{\alpha_t}{\alpha_s}\right) \boldsymbol{\mu} + \alpha_t \int_s^t g^2(\tau) \frac{\boldsymbol{\epsilon}_\theta(\mathbf{x}_\tau, \tau)}{\alpha_\tau \sigma_\tau} d\tau + \sqrt{- \int_s^t \frac{\alpha_t^2}{\alpha_\tau^2} g^2(\tau) d\tau} \mathbf{z}, \quad (31)$$

721 where  $\alpha_t := e^{- \int_0^t f(\tau) d\tau}$  and  $\mathbf{z} \sim \mathcal{N}(\mathbf{0}, \mathbf{I})$ .

722 *Proof.* For SDEs in the form of Eq.(1), Itô's formula gives the following conclusion:

$$724 \quad d\psi(\mathbf{x}, t) = \frac{\partial \psi(\mathbf{x}, t)}{\partial t} dt + \frac{\partial \psi(\mathbf{x}, t)}{\partial \mathbf{x}} [f(\mathbf{x}, t) dt + g(t) dw] + \frac{1}{2} \frac{\partial^2 \psi(\mathbf{x}, t)}{\partial \mathbf{x}^2} g^2(t) dt, \quad (32)$$

726 where  $\psi(\mathbf{x}, t)$  is a differentiable function. And we define

$$727 \quad \psi(\mathbf{x}, t) = \mathbf{x} e^{\int_0^t f(\tau) d\tau}$$

729 By substituting  $f(\mathbf{x}, t)$  and  $g(t)$  with the corresponding drift and diffusion coefficients in Eq.(10),  
 730 we obtain

$$731 \quad d\psi(\mathbf{x}, t) = \boldsymbol{\mu} f(t) e^{\int_0^t f(\tau) d\tau} dt + e^{\int_0^t f(\tau) d\tau} \left[ \frac{g^2(t)}{\sigma_t} \boldsymbol{\epsilon}_\theta(\mathbf{x}_t, t) dt + g(t) d\bar{w} \right].$$

734 And we integrate both sides of the above equation from  $s$  to  $t$ :

$$735 \quad \psi(\mathbf{x}, t) - \psi(\mathbf{x}, s) = \boldsymbol{\mu} (e^{\int_0^t f(\tau) d\tau} - e^{\int_0^s f(\tau) d\tau}) + \int_s^t e^{\int_0^\tau f(\xi) d\xi} g^2(\tau) \frac{\boldsymbol{\epsilon}_\theta(\mathbf{x}_\tau, \tau)}{\sigma_\tau} d\tau + \int_s^t e^{\int_0^\tau f(\xi) d\xi} g(\tau) d\bar{w}.$$

738 Note that  $\bar{w}$  is a standard Wiener process running backwards in time and we have the quadratic  
 739 variation  $(d\bar{w})^2 = -dt$ . According to the definition of  $\psi(\mathbf{x}, t)$  and  $\alpha_t$ , we have

$$740 \quad \frac{\mathbf{x}_t}{\alpha_t} - \frac{\mathbf{x}_s}{\alpha_s} = \boldsymbol{\mu} \left( \frac{1}{\alpha_t} - \frac{1}{\alpha_s} \right) + \int_s^t g^2(\tau) \frac{\boldsymbol{\epsilon}_\theta(\mathbf{x}_\tau, \tau)}{\alpha_\tau \sigma_\tau} d\tau + \sqrt{- \int_s^t \frac{g^2(\tau)}{\alpha_\tau^2} d\tau} \mathbf{z},$$

743 which is equivalent to Eq.(31).

744 **Proposition 2.** Given an initial value  $\mathbf{x}_s$  at time  $s \in [0, T]$ , the solution  $\mathbf{x}_t$  at time  $t \in [0, s]$  of  
 745 Eq.(15) is

$$746 \quad \mathbf{x}_t = \frac{\alpha_t}{\alpha_s} \mathbf{x}_s + \left(1 - \frac{\alpha_t}{\alpha_s}\right) \boldsymbol{\mu} + \alpha_t \int_s^t \frac{g^2(\tau)}{2\alpha_\tau \sigma_\tau} \boldsymbol{\epsilon}_\theta(\mathbf{x}_\tau, \tau) d\tau, \quad (33)$$

748 where  $\alpha_t := e^{- \int_0^t f(\tau) d\tau}$ .

750 *Proof.* For ODEs which have a semi-linear structure as follows:

$$751 \quad \frac{d\mathbf{x}}{dt} = P(t) \mathbf{x} + Q(\mathbf{x}, t), \quad (34)$$

753 the method of "variation of constants" gives the following solution:

$$755 \quad \mathbf{x}(t) = e^{\int_0^t P(\tau) d\tau} \cdot \left[ \int_0^t Q(\mathbf{x}, \tau) e^{- \int_0^\tau P(r) dr} d\tau + C \right].$$

756 By simultaneously considering the following two equations  
 757

$$\begin{cases} \mathbf{x}(t) = e^{\int_0^t P(\tau) d\tau} \cdot \left[ \int_0^t Q(\mathbf{x}, \tau) e^{-\int_0^\tau P(r) dr} d\tau + C \right], \\ \mathbf{x}(s) = e^{\int_0^s P(\tau) d\tau} \cdot \left[ \int_0^s Q(\mathbf{x}, \tau) e^{-\int_0^\tau P(r) dr} d\tau + C \right], \end{cases}$$

762 and eliminating  $C$ , we obtain  
 763

$$\mathbf{x}(t) = \mathbf{x}(s) e^{\int_s^t P(\tau) d\tau} + \int_s^t Q(\mathbf{x}, \tau) e^{\int_\tau^t P(\xi) d\xi} d\tau. \quad (35)$$

767 Now we compare Eq.(15) with Eq.(34) and let  
 768

$$\begin{aligned} P(t) &= -f(t) \\ \text{and } Q(\mathbf{x}, t) &= f(t)\boldsymbol{\mu} + \frac{g^2(t)}{2\sigma_t} \boldsymbol{\epsilon}_\theta(\mathbf{x}_t, t). \end{aligned}$$

773 Therefore, we can rewrite Eq.(35) as  
 774

$$\begin{aligned} \mathbf{x}_t &= \mathbf{x}_s e^{-\int_s^t f(\tau) d\tau} + \int_s^t e^{-\int_\tau^t f(\xi) d\xi} \left[ f(\tau)\boldsymbol{\mu} + \frac{g^2(\tau)}{2\sigma_\tau} \boldsymbol{\epsilon}_\theta(\mathbf{x}_\tau, \tau) \right] d\tau \\ &= \mathbf{x}_s e^{-\int_s^t f(\tau) d\tau} + \boldsymbol{\mu} (1 - e^{-\int_s^t f(\tau) d\tau}) + \int_s^t e^{-\int_\tau^t f(\xi) d\xi} \frac{g^2(\tau)}{2\sigma_\tau} \boldsymbol{\epsilon}_\theta(\mathbf{x}_\tau, \tau) d\tau, \end{aligned}$$

780 which is equivalent to Eq.(33).

782 **Proposition 3.** Given an initial value  $\mathbf{x}_s$  at time  $s \in [0, T]$ , the solution  $\mathbf{x}_t$  at time  $t \in [0, s]$  of  
 783 Eq.(22) is

$$\begin{aligned} \mathbf{x}_t &= \frac{\sigma_t}{\sigma_s} e^{-(\lambda_t - \lambda_s)} \mathbf{x}_s + \boldsymbol{\mu} \left( 1 - \frac{\alpha_t}{\alpha_s} e^{-2(\lambda_t - \lambda_s)} - \alpha_t + \alpha_t e^{-2(\lambda_t - \lambda_s)} \right) \\ &\quad + 2\alpha_t \int_{\lambda_s}^{\lambda_t} e^{-2(\lambda_t - \lambda)} \mathbf{x}_\lambda(\lambda) d\lambda + \sigma_t \sqrt{1 - e^{-2(\lambda_t - \lambda_s)}} \mathbf{z}, \end{aligned} \quad (36)$$

790 where  $\mathbf{z} \sim \mathcal{N}(\mathbf{0}, \mathbf{I})$ .

792 *Proof.* According to Eq.(32), we define

$$\begin{aligned} u(t) &= \frac{g^2(t)}{\sigma_t^2} - f(t) \\ \text{and } \psi(\mathbf{x}, t) &= \mathbf{x} e^{\int_0^t u(\tau) d\tau}. \end{aligned}$$

798 We substitute  $f(\mathbf{x}, t)$  and  $g(t)$  in Eq.(32) with the corresponding drift and diffusion coefficients in  
 799 Eq.(22), and integrate both sides of the equation from  $s$  to  $t$ :

$$\begin{aligned} \mathbf{x}_t &= \mathbf{x}_s e^{\int_s^t u(\tau) d\tau} + \boldsymbol{\mu} \int_s^t e^{\int_\tau^t u(\xi) d\xi} \left[ f(\tau) - \frac{g^2(\tau)}{\sigma_\tau^2} (1 - \alpha_\tau) \right] d\tau \\ &\quad - \int_s^t e^{\int_\tau^t u(\xi) d\xi} \left[ \frac{g^2(\tau)}{\sigma_\tau^2} \alpha_\tau \mathbf{x}_\tau(\tau) \right] d\tau + \int_s^t e^{\int_\tau^t u(\xi) d\xi} g(\tau) d\bar{w}. \end{aligned} \quad (37)$$

806 We can rewrite  $g(\tau)$  as Eq.(12) and obtain  
 807

$$e^{\int_s^t u(\tau) d\tau} = \exp \int_s^t \left( -2 \frac{d\lambda_\tau}{d\tau} - f(\tau) \right) d\tau = \frac{\alpha_t}{\alpha_s} e^{-2(\lambda_t - \lambda_s)} = \frac{\sigma_t}{\sigma_s} e^{-(\lambda_t - \lambda_s)}. \quad (38)$$

810 Next, we consider each term in Eq.(37) by employing Eq.(12) and Eq.(38). Firstly, we simplify the  
 811 second term:

$$\begin{aligned}
 & \boldsymbol{\mu} \int_s^t e^{\int_\tau^t u(\xi) d\xi} \left[ f(\tau) - \frac{g^2(\tau)}{\sigma_\tau^2} (1 - \alpha_\tau) \right] d\tau \\
 &= \boldsymbol{\mu} \int_s^t \frac{\sigma_t}{\sigma_\tau} e^{-(\lambda_t - \lambda_\tau)} \left[ f(\tau) + 2(1 - \alpha_\tau) \frac{d\lambda_\tau}{d\tau} \right] d\tau \\
 &= \boldsymbol{\mu} \sigma_t e^{-\lambda_t} \int_s^t \frac{e^{\lambda_\tau}}{\sigma_\tau} [f(\tau) d\tau + 2(1 - \alpha_\tau) d\lambda_\tau] \\
 &= \boldsymbol{\mu} \sigma_t e^{-\lambda_t} \int_s^t \frac{\alpha_\tau}{\sigma_\tau^2} [f(\tau) d\tau + 2d\lambda_\tau - 2\alpha_\tau d\lambda_\tau] \\
 &= \boldsymbol{\mu} \sigma_t e^{-\lambda_t} \int_s^t \frac{-d\alpha_\tau}{\sigma_\tau^2} + \frac{2\alpha_\tau}{\sigma_\tau^2} d\lambda_\tau - 2 \frac{\alpha_\tau^2}{\sigma_\tau^2} d\lambda_\tau. \tag{39}
 \end{aligned}$$

825 Note that

$$d\lambda_t = d\left(\log \frac{\alpha_t}{\sigma_\infty \sqrt{1 - \alpha_t^2}}\right) = \frac{d\alpha_t}{\alpha_t} + \frac{\alpha_t d\alpha_t}{1 - \alpha_t^2} = \frac{d\alpha_t}{\alpha_t(1 - \alpha_t^2)}. \tag{40}$$

828 Substitute Eq.(40) into Eq.(39) and we obtain

$$\begin{aligned}
 & \boldsymbol{\mu} \int_s^t e^{\int_\tau^t u(\xi) d\xi} \left[ f(\tau) - \frac{g^2(\tau)}{\sigma_\tau^2} (1 - \alpha_\tau) \right] d\tau \\
 &= \boldsymbol{\mu} \sigma_t e^{-\lambda_t} \int_s^t \frac{-d\alpha_\tau}{\sigma_\tau^2} + \frac{2d\alpha_\tau}{\sigma_\tau^2(1 - \alpha_\tau^2)} - 2 \frac{\alpha_\tau^2}{\sigma_\tau^2} d\lambda_\tau \\
 &= \boldsymbol{\mu} \sigma_t e^{-\lambda_t} \int_s^t \frac{1 + \alpha_\tau^2}{\sigma_\infty^2 (1 - \alpha_\tau^2)^2} d\alpha_\tau - 2e^{2\lambda_\tau} d\lambda_\tau \\
 &= \boldsymbol{\mu} \sigma_t e^{-\lambda_t} \int_s^t \frac{1}{\sigma_\infty^2} d\left(\frac{\alpha_\tau}{1 - \alpha_\tau^2}\right) - 2e^{2\lambda_\tau} d\lambda \\
 &= \boldsymbol{\mu} \left( 1 - \frac{\alpha_t}{\alpha_s} e^{-2(\lambda_t - \lambda_s)} - \alpha_t + \alpha_t e^{-2(\lambda_t - \lambda_s)} \right). \tag{41}
 \end{aligned}$$

842 Secondly, we rewrite the third term in Eq.(37) by employing Eq.(12) and Eq.(38).

$$\begin{aligned}
 - \int_s^t e^{\int_\tau^t u(\xi) d\xi} \left[ \frac{g^2(\tau)}{\sigma_\tau^2} \alpha_\tau \mathbf{x}_\theta(\mathbf{x}_\tau, \tau) \right] d\tau &= - \int_s^t \frac{\sigma_t}{\sigma_\tau} e^{-(\lambda_t - \lambda_\tau)} \left[ -2 \frac{d\lambda_\tau}{d\tau} \alpha_\tau \mathbf{x}_\theta(\mathbf{x}_\tau, \tau) \right] d\tau \\
 &= 2 \int_s^t \sigma_t e^{2\lambda_\tau - \lambda_t} \mathbf{x}_\theta(\mathbf{x}_\tau, \lambda_\tau) d\lambda_\tau \\
 &= 2\alpha_t \int_{\lambda_s}^{\lambda_t} e^{-2(\lambda_t - \lambda)} \mathbf{x}_\theta(\mathbf{x}_\lambda, \lambda) d\lambda. \tag{42}
 \end{aligned}$$

851 Thirdly, we consider the fourth term in Eq.(37) (note that  $(d\bar{\mathbf{w}})^2 = -d\tau$ ):

$$\begin{aligned}
 \int_s^t e^{\int_\tau^t u(\xi) d\xi} g(\tau) d\bar{\mathbf{w}} &= \sqrt{- \int_s^t e^{2 \int_\tau^t u(\xi) d\xi} g^2(\tau) d\tau} \mathbf{z} \\
 &= \sqrt{- \int_s^t \frac{\sigma_t^2}{\sigma_\tau^2} e^{-2(\lambda_t - \lambda_\tau)} \left( -2\sigma_\tau^2 \frac{d\lambda_\tau}{d\tau} \right) d\tau} \mathbf{z} \\
 &= \sqrt{\sigma_t^2 \int_s^t 2e^{2(\lambda_\tau - \lambda_t)} d\lambda_\tau} \mathbf{z} \\
 &= \sigma_t \sqrt{1 - e^{-2(\lambda_t - \lambda_s)}} \mathbf{z}. \tag{43}
 \end{aligned}$$

863 Lastly, we substitute Eq.(38) and Eq.(41-43) into Eq.(37) and obtain the solution as presented in  
 Eq.(36).

864     **Proposition 4.** Given an initial value  $\mathbf{x}_s$  at time  $s \in [0, T]$ , the solution  $\mathbf{x}_t$  at time  $t \in [0, s]$  of  
 865     Eq.(24) is

$$866 \quad \mathbf{x}_t = \frac{\sigma_t}{\sigma_s} \mathbf{x}_s + \boldsymbol{\mu} \left( 1 - \frac{\sigma_t}{\sigma_s} + \frac{\sigma_t}{\sigma_s} \alpha_s - \alpha_t \right) + \sigma_t \int_{\lambda_s}^{\lambda_t} e^\lambda \mathbf{x}_\theta(\mathbf{x}_\lambda, \lambda) d\lambda. \quad (44)$$

867     *Proof.* Note that Eq.(24) shares the same structure as Eq.(34). Let

$$868 \quad P(t) = \frac{g^2(t)}{2\sigma_t^2} - f(t), \\ 869 \quad \text{and } Q(\mathbf{x}, t) = \left[ f(t) - \frac{g^2(t)}{2\sigma_t^2} (1 - \alpha_t) \right] \boldsymbol{\mu} - \frac{g^2(t)}{2\sigma_t^2} \alpha_t \mathbf{x}_\theta(\mathbf{x}_t, t).$$

870     According to Eq.(12), we first consider

$$871 \quad e^{\int_s^t P(\tau) d\tau} = \exp \int_s^t \left[ \frac{g^2(\tau)}{2\sigma_\tau^2} - f(\tau) \right] d\tau = \exp \int_s^t -d\lambda_\tau + d\log \alpha_\tau \\ 872 \quad = \exp \int_s^t d\log \alpha_\tau - d\log \frac{\alpha_\tau}{\sigma_\tau} = \exp \int_s^t d\log \sigma_\tau = \frac{\sigma_t}{\sigma_s}. \quad (45)$$

873     Then, we can rewrite Eq.(35) as

$$874 \quad \mathbf{x}_t = \frac{\sigma_t}{\sigma_s} \mathbf{x}_s + \boldsymbol{\mu} \int_s^t \frac{\sigma_t}{\sigma_\tau} \left[ f(\tau) - \frac{g^2(\tau)}{2\sigma_\tau^2} (1 - \alpha_\tau) \right] d\tau - \int_s^t \frac{\sigma_t}{\sigma_\tau} \frac{g^2(\tau)}{2\sigma_\tau^2} \alpha_\tau \mathbf{x}_\theta(\mathbf{x}_\tau, \tau) d\tau. \quad (46)$$

875     Firstly, we consider the second term in Eq.(46)

$$876 \quad \boldsymbol{\mu} \int_s^t \frac{\sigma_t}{\sigma_\tau} \left[ f(\tau) - \frac{g^2(\tau)}{2\sigma_\tau^2} (1 - \alpha_\tau) \right] d\tau \\ 877 \quad = \boldsymbol{\mu} \sigma_t \int_s^t \frac{1}{\sigma_\tau} \left[ f(\tau) - \frac{g^2(\tau)}{2\sigma_\tau^2} + \frac{g^2(\tau)}{2\sigma_\tau^2} \alpha_\tau \right] d\tau \\ 878 \quad = \boldsymbol{\mu} \sigma_t \left[ \int_s^t \frac{1}{\sigma_\tau} \left( f(\tau) - \frac{g^2(\tau)}{2\sigma_\tau^2} \right) d\tau + \int_s^t \frac{g^2(\tau)}{2\sigma_\tau^3} \alpha_\tau d\tau \right] \\ 879 \quad = \boldsymbol{\mu} \sigma_t \left[ - \int_s^t \frac{d\log \sigma_\tau}{\sigma_\tau} - \int_s^t \frac{\alpha_\tau}{\sigma_\tau} d\lambda_\tau \right] \quad (\text{refer to Eq.(12) and Eq.(45)}) \\ 880 \quad = \boldsymbol{\mu} \sigma_t \left[ \int_s^t d\left( \frac{1}{\sigma_\tau} \right) - \int_s^t de^{\lambda_\tau} \right] \\ 881 \quad = \boldsymbol{\mu} \left( 1 - \frac{\sigma_t}{\sigma_s} + \frac{\sigma_t}{\sigma_s} \alpha_s - \alpha_t \right). \quad (47)$$

882     Secondly, we rewrite the third term in Eq.(46)

$$883 \quad - \int_s^t \frac{\sigma_t}{\sigma_\tau} \frac{g^2(\tau)}{2\sigma_\tau^2} \alpha_\tau \mathbf{x}_\theta(\mathbf{x}_\tau, \tau) d\tau = \sigma_t \int_s^t e^{\lambda_\tau} \mathbf{x}_\theta(\mathbf{x}_\lambda, \lambda) d\lambda_\tau. \quad (48)$$

884     By substituting Eq.(47) and Eq.(48) into Eq.(46), we can obtain the solution shown in Eq.(44).

## 906 A.2 EQUIVALENCE BETWEEN POSTERIOR SAMPLING AND EULER-MARUYAMA 907 DISCRETIZATION

908     The *posterior sampling* (Luo et al., 2024b) algorithm utilizes the reparameterization of Gaussian  
 909 distribution in Eq.(19) and computes  $\mathbf{x}_{i-1}$  from  $\mathbf{x}_i$  iteratively as follows:

$$910 \quad \mathbf{x}_{i-1} = \tilde{\boldsymbol{\mu}}_i(\mathbf{x}_i, \mathbf{x}_0) + \sqrt{\tilde{\beta}_i} \mathbf{z}_i, \\ 911 \quad \tilde{\boldsymbol{\mu}}_i(\mathbf{x}_i, \mathbf{x}_0) = \frac{(1 - \alpha_{i-1}^2)\alpha_i}{(1 - \alpha_i^2)\alpha_{i-1}} (\mathbf{x}_i - \boldsymbol{\mu}) + \frac{1 - \frac{\alpha_i^2}{\alpha_{i-1}^2}}{1 - \alpha_i^2} \alpha_{i-1} (\mathbf{x}_0 - \boldsymbol{\mu}) + \boldsymbol{\mu}, \\ 912 \quad \tilde{\beta}_i = \frac{(1 - \alpha_{i-1}^2)(1 - \frac{\alpha_i^2}{\alpha_{i-1}^2})}{1 - \alpha_i^2}, \quad (49)$$

918 where  $\mathbf{z}_i \sim \mathcal{N}(\mathbf{0}, \mathbf{I})$ ,  $\alpha_i = e^{-\int_0^i f(\tau) d\tau}$  and  $\mathbf{x}_0 = (\mathbf{x}_i - \boldsymbol{\mu} - \sigma_i \boldsymbol{\epsilon}_\theta(\mathbf{x}_i, \boldsymbol{\mu}, t_i)) / \alpha_i + \boldsymbol{\mu}$ . By substituting  $\mathbf{x}_0$  into  $\tilde{\boldsymbol{\mu}}_i$ , we arrange the equation and obtain

$$\begin{aligned} \tilde{\boldsymbol{\mu}}_i(\mathbf{x}_i, \mathbf{x}_0) &= \frac{\alpha_{i-1}}{\alpha_i} \mathbf{x}_i + \left(1 - \frac{\alpha_{i-1}}{\alpha_i}\right) \boldsymbol{\mu} - \frac{\frac{\alpha_{i-1}}{\alpha_i} - \frac{\alpha_i}{\alpha_{i-1}}}{1 - \alpha_i^2} \sigma_i \tilde{\boldsymbol{\epsilon}}_\theta(\mathbf{x}_i, \boldsymbol{\mu}, t_i) \\ &= \frac{\alpha_{i-1}}{\alpha_i} \mathbf{x}_i + \left(1 - \frac{\alpha_{i-1}}{\alpha_i}\right) \boldsymbol{\mu} - \frac{\frac{\alpha_{i-1}}{\alpha_i} - \frac{\alpha_i}{\alpha_{i-1}}}{\sqrt{1 - \alpha_i^2}} \sigma_\infty \tilde{\boldsymbol{\epsilon}}_\theta(\mathbf{x}_i, \boldsymbol{\mu}, t_i). \end{aligned} \quad (50)$$

We note that

$$\frac{\alpha_{i-1}}{\alpha_i} = e^{\int_{i-1}^i f(\tau) d\tau} = 1 + \int_{i-1}^i f(\tau) d\tau + o\left(\int_{i-1}^i f(\tau) d\tau\right) \approx 1 + f(t_i) \Delta t_i, \quad (51)$$

where the high-order error term is omitted and  $\Delta t_i := t_i - t_{i-1}$ . By substituting Eq.(51) into Eq.(50) and Eq.(49), we obtain

$$\tilde{\boldsymbol{\mu}}_i(\mathbf{x}_i, \mathbf{x}_0) = (1 + f(t_i) \Delta t_i) \mathbf{x}_i - f(t_i) \Delta t_i \boldsymbol{\mu} - \frac{2f(t_i) \Delta t_i \sigma_\infty}{\sqrt{1 - \alpha_i^2}} \tilde{\boldsymbol{\epsilon}}_\theta(\mathbf{x}_i, \boldsymbol{\mu}, t_i), \quad (52)$$

$$\tilde{\beta}_i = \frac{(1 - \alpha_{i-1}^2)(1 - \frac{\alpha_i^2}{\alpha_{i-1}^2})}{1 - \alpha_i^2} \approx \frac{2f(t_i) \Delta t_i (1 - \alpha_{i-1}^2)}{1 - \alpha_i^2}. \quad (53)$$

On the other hand, the reverse-time SDE has been presented in Eq.(10). Combining the assumption  $g^2(t)/f(t) = 2\sigma_\infty^2$  in Section 2.2 and the definition of  $\sigma_t$  in Section 3.1, the Euler–Maruyama descretization of this SDE is

$$\begin{aligned} \mathbf{x}_{i-1} - \mathbf{x}_i &= -f(t_i)(\boldsymbol{\mu} - \mathbf{x}_i) \Delta t_i - \frac{g^2(t_i)}{\sigma_i} \tilde{\boldsymbol{\epsilon}}_\theta(\mathbf{x}_i, \boldsymbol{\mu}, t_i) \Delta t_i + g(t_i) \sqrt{\Delta t_i} \mathbf{z}_i, \\ \therefore \mathbf{x}_{i-1} &= (1 + f(t_i) \Delta t_i) \mathbf{x}_i - f(t_i) \Delta t_i \boldsymbol{\mu} - \frac{2\sigma_\infty^2 f(t_i)}{\sigma_\infty \sqrt{1 - \alpha_i^2}} \tilde{\boldsymbol{\epsilon}}_\theta(\mathbf{x}_i, \boldsymbol{\mu}, t_i) \Delta t_i + g(t_i) \sqrt{\Delta t_i} \mathbf{z}_i \\ &= (1 + f(t_i) \Delta t_i) \mathbf{x}_i - f(t_i) \Delta t_i \boldsymbol{\mu} - \frac{2f(t_i) \Delta t_i \sigma_\infty}{\sqrt{1 - \alpha_i^2}} \tilde{\boldsymbol{\epsilon}}_\theta(\mathbf{x}_i, \boldsymbol{\mu}, t_i) + \sigma_\infty \sqrt{2f(t_i) \Delta t_i} \mathbf{z}_i \\ &= \tilde{\boldsymbol{\mu}}_i(\mathbf{x}_i, \mathbf{x}_0) + \sigma_\infty \sqrt{\frac{1 - \alpha_i^2}{1 - \alpha_{i-1}^2}} \tilde{\beta}_i \mathbf{z}_i. \end{aligned} \quad (54)$$

Thus, the *posterior sampling* algorithm is a special Euler–Maruyama descretization of reverse-time SDE with a different coefficient of Gaussian noise.

### A.3 DERIVATIONS ABOUT VELOCITY PREDICTION

Following Eq.(27), We can define the *velocity prediction* as

$$\mathbf{v}_\theta(t) = \boldsymbol{\mu} \sin \phi_t - \mathbf{x}_\theta(t) \sin \phi_t + \sigma_\infty \cos(\phi_t) \boldsymbol{\epsilon}_\theta(t). \quad (55)$$

And we have the relationship between  $\mathbf{x}_\theta(t)$  and  $\boldsymbol{\epsilon}_\theta(t)$  as follows:

$$\mathbf{x}_t = \mathbf{x}_\theta(t) \cos \phi_t + \boldsymbol{\mu} (1 - \cos \phi_t) + \sigma_\infty \sin(\phi_t) \boldsymbol{\epsilon}_\theta(t). \quad (56)$$

In order to get  $\mathbf{x}_\theta$  from  $\mathbf{v}_\theta$ , we rewrite Eq.(55) as

$$\mathbf{x}_\theta(t) \sin^2 \phi_t = \boldsymbol{\mu} \sin^2 \phi_t - \mathbf{v}_\theta(t) \sin \phi_t + \sigma_\infty \boldsymbol{\epsilon}_\theta(t) \sin \phi_t \cos \phi_t. \quad (57)$$

Then we replace  $\boldsymbol{\epsilon}_\theta(t)$  according to Eq.(56)

$$\begin{aligned} \mathbf{x}_\theta(t) \sin^2 \phi_t &= \boldsymbol{\mu} \sin^2 \phi_t - \mathbf{v}_\theta(t) \sin \phi_t + [\mathbf{x}_t - \mathbf{x}_\theta(t) \cos \phi_t - \boldsymbol{\mu} (1 - \cos \phi_t)] \cos \phi_t \\ &= (1 - \cos \phi_t) \boldsymbol{\mu} - \mathbf{v}_\theta(t) \sin \phi_t + \mathbf{x}_t \cos \phi_t - \mathbf{x}_\theta(t) \cos^2 \phi_t. \end{aligned} \quad (58)$$

Arranging the above equation, we can obtain the transformation from  $\mathbf{v}_\theta$  to  $\mathbf{x}_\theta$ , as shown in Eq.(28). Similarly, we can also rewrite Eq.(55) and replace  $\mathbf{x}_\theta(t)$  as follows:

$$\begin{aligned} \sigma_\infty \cos^2(\phi_t) \boldsymbol{\epsilon}_\theta(t) &= \mathbf{v}_\theta(t) \cos \phi_t - \boldsymbol{\mu} \sin \phi_t \cos \phi_t + \mathbf{x}_\theta(t) \sin \phi_t \cos \phi_t \\ &= \mathbf{v}_\theta(t) \cos \phi_t - \boldsymbol{\mu} \sin \phi_t \cos \phi_t + \sin \phi_t [\mathbf{x}_t - \boldsymbol{\mu} (1 - \cos \phi_t) - \sigma_\infty \sin(\phi_t) \boldsymbol{\epsilon}_\theta(t)] \\ &= \mathbf{v}_\theta(t) \cos \phi_t - \boldsymbol{\mu} \sin \phi_t + \mathbf{x}_\theta(t) \sin \phi_t - \sigma_\infty \sin^2 \phi_t \boldsymbol{\epsilon}_\theta(t). \end{aligned} \quad (59)$$

Thus we obtain the transformation from  $\mathbf{v}_\theta$  to  $\boldsymbol{\epsilon}_\theta$ , as presented in Eq.(29).

972 **B NOTATION COMPARISON TABLE**  
973  
974  
975  
976

---

This paper	$f(t)$	$g(t)$	$\alpha_t$	$\sigma_t$
MRSDE (Luo et al., 2023b)	$\theta_t$	$\sigma_t$	$e^{-\int_0^t \theta_\tau d\tau}$	$\sigma_\infty \sqrt{1 - e^{-2 \int_0^t \theta_\tau d\tau}}$

---

981 Table 4: The correspondence between the notations used in this paper (left column) and notations  
982 used by MRSDE (right column).  
983  
984  
985  
986  
987

988 **C DETAILED SAMPLING ALGORITHM OF MR SAMPLER**  
989  
990

991 We list the detailed MR Sampler algorithm with different solvers, parameterizations and orders as  
992 follows.  
993

994 **Algorithm 1** MR Sampler-SDE-n-1.  
995

996 **Require:** initial value  $\mathbf{x}_T = \boldsymbol{\mu} + \sigma_\infty \boldsymbol{\epsilon}$ , Gaussian noise sequence  $\{\mathbf{z}_i | \mathbf{z}_i \sim \mathcal{N}(\mathbf{0}, \mathbf{I})\}_{i=1}^M$ , time steps  
997  $\{t_i\}_{i=0}^M$ , data prediction model  $\mathbf{x}_\theta$ . Denote  $h_i := \lambda_{t_i} - \lambda_{t_{i-1}}$  for  $i = 1, \dots, M$ .  
998 1:  $\mathbf{x}_{t_0} \leftarrow \mathbf{x}_T$ . Initialize an empty buffer  $Q$ .  
999 2:  $Q \xleftarrow{\text{buffer}} \mathbf{x}_\theta(\mathbf{x}_{t_0}, t_0)$   
1000 3: **for**  $i \leftarrow 1$  to  $M$  **do**  
1001   4:  $\mathbf{x}_{t_i} = \frac{\alpha_{t_i}}{\alpha_{t_{i-1}}} \mathbf{x}_{t_{i-1}} + \left(1 - \frac{\alpha_{t_i}}{\alpha_{t_{i-1}}}\right) \boldsymbol{\mu} - 2\sigma_{t_i}(e^{h_i} - 1)\boldsymbol{\epsilon}_\theta(\mathbf{x}_{t_{i-1}}, t_{i-1}) + \sigma_{t_i} \sqrt{e^{2h_i} - 1} \mathbf{z}_i$   
1002   5: If  $i < M$ , then  $Q \xleftarrow{\text{buffer}} \mathbf{x}_\theta(\mathbf{x}_{t_i}, t_i)$   
1003   6: **end for**  
1004 7: **return**  $\mathbf{x}_{t_M}$ 


---

1005  
1006  
1007  
1008  
1009

1010 **Algorithm 2** MR Sampler-SDE-n-2.  
1011

1012 **Require:** initial value  $\mathbf{x}_T = \boldsymbol{\mu} + \sigma_\infty \boldsymbol{\epsilon}$ , Gaussian noise sequence  $\{\mathbf{z}_i | \mathbf{z}_i \sim \mathcal{N}(\mathbf{0}, \mathbf{I})\}_{i=1}^M$ , time steps  
1013  $\{t_i\}_{i=0}^M$ , data prediction model  $\mathbf{x}_\theta$ . Denote  $h_i := \lambda_{t_i} - \lambda_{t_{i-1}}$  for  $i = 1, \dots, M$ .  
1014 1:  $\mathbf{x}_{t_0} \leftarrow \mathbf{x}_T$ . Initialize an empty buffer  $Q$ .  
1015 2:  $Q \xleftarrow{\text{buffer}} \mathbf{x}_\theta(\mathbf{x}_{t_0}, t_0)$   
1016 3:  $\mathbf{x}_{t_1} = \frac{\alpha_{t_1}}{\alpha_{t_0}} \mathbf{x}_{t_0} + \left(1 - \frac{\alpha_{t_1}}{\alpha_{t_0}}\right) \boldsymbol{\mu} - 2\sigma_{t_1}(e^{h_1} - 1)\boldsymbol{\epsilon}_\theta(\mathbf{x}_{t_0}, t_0) + \sigma_{t_1} \sqrt{e^{2h_1} - 1} \mathbf{z}_1$   
1017 4:  $Q \xleftarrow{\text{buffer}} \mathbf{x}_\theta(\mathbf{x}_{t_1}, t_1)$   
1018 5: **for**  $i \leftarrow 2$  to  $M$  **do**  
1019   6:  $\mathbf{D}_i = \frac{\boldsymbol{\epsilon}_\theta(\mathbf{x}_{t_{i-1}}, t_{i-1}) - \boldsymbol{\epsilon}_\theta(\mathbf{x}_{t_{i-2}}, t_{i-2})}{h_{i-1}}$   
1020   7:  $\mathbf{x}_{t_i} = \frac{\alpha_{t_i}}{\alpha_{t_{i-1}}} \mathbf{x}_{t_{i-1}} + \left(1 - \frac{\alpha_{t_i}}{\alpha_{t_{i-1}}}\right) \boldsymbol{\mu} - 2\sigma_{t_i} [(e^{h_i} - 1)\boldsymbol{\epsilon}_\theta(\mathbf{x}_{t_{i-1}}, t_{i-1}) + (e^{h_i} - 1 - h_i)\mathbf{D}_i] +$   
1021      $\sigma_{t_i} \sqrt{e^{2h_i} - 1} \mathbf{z}_i$   
1022   8: If  $i < M$ , then  $Q \xleftarrow{\text{buffer}} \mathbf{x}_\theta(\mathbf{x}_{t_i}, t_i)$   
1023   9: **end for**  
1024 10: **return**  $\mathbf{x}_{t_M}$ 


---

1025

---

1026   **Algorithm 3** MR Sampler-ODE-n-1.

---

1027  
**Require:** initial value  $\mathbf{x}_T = \boldsymbol{\mu} + \sigma_\infty \boldsymbol{\epsilon}$ , time steps  $\{t_i\}_{i=0}^M$ , data prediction model  $\mathbf{x}_\theta$ . Denote  
 $h_i := \lambda_{t_i} - \lambda_{t_{i-1}}$  for  $i = 1, \dots, M$ .

1028   1:  $\mathbf{x}_{t_0} \leftarrow \mathbf{x}_T$ . Initialize an empty buffer  $Q$ .

1029   2:  $Q \xleftarrow{\text{buffer}} \mathbf{x}_\theta(\mathbf{x}_{t_0}, t_0)$

1030   3: **for**  $i \leftarrow 1$  to  $M$  **do**

1031     4:  $\mathbf{x}_{t_i} = \frac{\alpha_{t_i}}{\alpha_{t_{i-1}}} \mathbf{x}_{t_{i-1}} + \left(1 - \frac{\alpha_{t_i}}{\alpha_{t_{i-1}}}\right) \boldsymbol{\mu} - \sigma_{t_i} (e^{h_i} - 1) \boldsymbol{\epsilon}_\theta(\mathbf{x}_{t_{i-1}}, t_{i-1})$

1032     5: If  $i < M$ , then  $Q \xleftarrow{\text{buffer}} \mathbf{x}_\theta(\mathbf{x}_{t_i}, t_i)$

1033     6: **end for**

1034   7: **return**  $\mathbf{x}_{t_M}$

---

1038  
1039  
1040  
1041  
1042  
1043  
1044

1045   **Algorithm 4** MR Sampler-ODE-n-2.

---

1046  
**Require:** initial value  $\mathbf{x}_T = \boldsymbol{\mu} + \sigma_\infty \boldsymbol{\epsilon}$ , time steps  $\{t_i\}_{i=0}^M$ , data prediction model  $\mathbf{x}_\theta$ . Denote  
 $h_i := \lambda_{t_i} - \lambda_{t_{i-1}}$  for  $i = 1, \dots, M$ .

1047   1:  $\mathbf{x}_{t_0} \leftarrow \mathbf{x}_T$ . Initialize an empty buffer  $Q$ .

1048   2:  $Q \xleftarrow{\text{buffer}} \mathbf{x}_\theta(\mathbf{x}_{t_0}, t_0)$

1049   3:  $\mathbf{x}_{t_1} = \frac{\alpha_{t_1}}{\alpha_{t_0}} \mathbf{x}_{t_0} + \left(1 - \frac{\alpha_{t_1}}{\alpha_{t_0}}\right) \boldsymbol{\mu} - \sigma_{t_1} (e^{h_1} - 1) \boldsymbol{\epsilon}_\theta(\mathbf{x}_{t_0}, t_0)$

1050   4:  $Q \xleftarrow{\text{buffer}} \mathbf{x}_\theta(\mathbf{x}_{t_1}, t_1)$

1051   5: **for**  $i \leftarrow 2$  to  $M$  **do**

1052     6:  $\mathbf{D}_i = \frac{\boldsymbol{\epsilon}_\theta(\mathbf{x}_{t_{i-1}}, t_{i-1}) - \boldsymbol{\epsilon}_\theta(\mathbf{x}_{t_{i-2}}, t_{i-2})}{h_{i-1}}$

1053     7:  $\mathbf{x}_{t_i} = \frac{\alpha_{t_i}}{\alpha_{t_{i-1}}} \mathbf{x}_{t_{i-1}} + \left(1 - \frac{\alpha_{t_i}}{\alpha_{t_{i-1}}}\right) \boldsymbol{\mu} - \sigma_{t_i} [(e^{h_i} - 1) \boldsymbol{\epsilon}_\theta(\mathbf{x}_{t_{i-1}}, t_{i-1}) + (e^{h_i} - 1 - h_i) \mathbf{D}_i]$

1054     8: If  $i < M$ , then  $Q \xleftarrow{\text{buffer}} \mathbf{x}_\theta(\mathbf{x}_{t_i}, t_i)$

1055     9: **end for**

1056   10: **return**  $\mathbf{x}_{t_M}$

---

1061  
1062  
1063  
1064  
1065  
1066  
1067

1068   **Algorithm 5** MR Sampler-SDE-d-1.

---

1069  
**Require:** initial value  $\mathbf{x}_T = \boldsymbol{\mu} + \sigma_\infty \boldsymbol{\epsilon}$ , Gaussian noise sequence  $\{\mathbf{z}_i | \mathbf{z}_i \sim \mathcal{N}(\mathbf{0}, \mathbf{I})\}_{i=1}^M$ , time steps  
 $\{t_i\}_{i=0}^M$ , data prediction model  $\mathbf{x}_\theta$ . Denote  $h_i := \lambda_{t_i} - \lambda_{t_{i-1}}$  for  $i = 1, \dots, M$ .

1070   1:  $\mathbf{x}_{t_0} \leftarrow \mathbf{x}_T$ . Initialize an empty buffer  $Q$ .

1071   2:  $Q \xleftarrow{\text{buffer}} \mathbf{x}_\theta(\mathbf{x}_{t_0}, t_0)$

1072   3: **for**  $i \leftarrow 1$  to  $M$  **do**

1073     4:  $\mathbf{x}_{t_i} = \frac{\sigma_{t_i}}{\sigma_{t_{i-1}}} e^{-h_i} \mathbf{x}_{t_{i-1}} + \boldsymbol{\mu} \left(1 - \frac{\sigma_{t_i}}{\sigma_{t_{i-1}}} e^{-2h_i} - \alpha_{t_i} + \alpha_{t_i} e^{-2h_i}\right) + \sigma_{t_i} \sqrt{1 - e^{-2h_i}} \mathbf{z}_i +$   
 $\alpha_{t_i} (1 - e^{-2h_i}) \mathbf{x}_\theta(\mathbf{x}_{t_{i-1}}, t_{i-1})$

1074     5: If  $i < M$ , then  $Q \xleftarrow{\text{buffer}} \mathbf{x}_\theta(\mathbf{x}_{t_i}, t_i)$

1075     6: **end for**

1076   7: **return**  $\mathbf{x}_{t_M}$

---

---

1080   **Algorithm 6** MR Sampler-SDE-d-2.

---

1081   **Require:** initial value  $\mathbf{x}_T = \boldsymbol{\mu} + \sigma_\infty \boldsymbol{\epsilon}$ , Gaussian noise sequence  $\{\mathbf{z}_i | \mathbf{z}_i \sim \mathcal{N}(\mathbf{0}, \mathbf{I})\}_{i=1}^M$ , time steps  
1082     $\{t_i\}_{i=0}^M$ , data prediction model  $\mathbf{x}_\theta$ . Denote  $h_i := \lambda_{t_i} - \lambda_{t_{i-1}}$  for  $i = 1, \dots, M$ .

1083   1:  $\mathbf{x}_{t_0} \leftarrow \mathbf{x}_T$ . Initialize an empty buffer  $Q$ .

1084   2:  $Q \xleftarrow{\text{buffer}} \mathbf{x}_\theta(\mathbf{x}_{t_0}, t_0)$

1085   3:  $\mathbf{x}_{t_1} = \frac{\sigma_{t_1}}{\sigma_{t_0}} e^{-h_1} \mathbf{x}_{t_0} + \boldsymbol{\mu} \left(1 - \frac{\alpha_{t_1}}{\alpha_{t_0}} e^{-2h_1} - \alpha_{t_1} + \alpha_{t_1} e^{-2h_1}\right) + \alpha_{t_1} (1 - e^{-2h_1}) \mathbf{x}_\theta(\mathbf{x}_{t_0}, t_0) +$   
1086     $\sigma_{t_1} \sqrt{1 - e^{-2h_1}} \mathbf{z}_1$

1087   4:  $Q \xleftarrow{\text{buffer}} \mathbf{x}_\theta(\mathbf{x}_{t_1}, t_1)$

1088   5: **for**  $i \leftarrow 2$  to  $M$  **do**

1089    6:  $D_i = \frac{\mathbf{x}_\theta(\mathbf{x}_{t_{i-1}}, t_{i-1}) - \mathbf{x}_\theta(\mathbf{x}_{t_{i-2}}, t_{i-2})}{h_{i-1}}$

1090    7:  $\mathbf{x}_{t_i} = \frac{\sigma_{t_i}}{\sigma_{t_{i-1}}} e^{-h_i} \mathbf{x}_{t_{i-1}} + \boldsymbol{\mu} \left(1 - \frac{\alpha_{t_i}}{\alpha_{t_{i-1}}} e^{-2h_i} - \alpha_{t_i} + \alpha_{t_i} e^{-2h_i}\right) + \sigma_{t_i} \sqrt{1 - e^{-2h_i}} \mathbf{z}_i +$   
1091     $\alpha_{t_i} (1 - e^{-2h_i}) \mathbf{x}_\theta(\mathbf{x}_{t_{i-1}}, t_{i-1}) + \alpha_{t_i} \left(h_i - \frac{1 - e^{-2h_i}}{2}\right) D_i$

1092    8: If  $i < M$ , then  $Q \xleftarrow{\text{buffer}} \mathbf{x}_\theta(\mathbf{x}_{t_i}, t_i)$

1093   9: **end for**

1094   10: **return**  $\mathbf{x}_{t_M}$

---

1095  
1096  
1097  
1098  
1099  
1100  
1101  
1102

1103   **Algorithm 7** MR Sampler-ODE-d-1.

---

1104   **Require:** initial value  $\mathbf{x}_T = \boldsymbol{\mu} + \sigma_\infty \boldsymbol{\epsilon}$ , time steps  $\{t_i\}_{i=0}^M$ , data prediction model  $\mathbf{x}_\theta$ . Denote  
1105     $h_i := \lambda_{t_i} - \lambda_{t_{i-1}}$  for  $i = 1, \dots, M$ .

1106   1:  $\mathbf{x}_{t_0} \leftarrow \mathbf{x}_T$ . Initialize an empty buffer  $Q$ .

1107   2:  $Q \xleftarrow{\text{buffer}} \mathbf{x}_\theta(\mathbf{x}_{t_0}, t_0)$

1108   3: **for**  $i \leftarrow 1$  to  $M$  **do**

1109    4:  $\mathbf{x}_{t_i} = \frac{\sigma_{t_i}}{\sigma_{t_{i-1}}} \mathbf{x}_{t_{i-1}} + \boldsymbol{\mu} \left(1 - \frac{\sigma_{t_i}}{\sigma_{t_{i-1}}} + \frac{\sigma_{t_i}}{\sigma_{t_{i-1}}} \alpha_{t_{i-1}} - \alpha_{t_i}\right) + \alpha_{t_i} (1 - e^{-h_i}) \mathbf{x}_\theta(\mathbf{x}_{t_{i-1}}, t_{i-1})$

1110    5: If  $i < M$ , then  $Q \xleftarrow{\text{buffer}} \mathbf{x}_\theta(\mathbf{x}_{t_i}, t_i)$

1111   6: **end for**

1112   7: **return**  $\mathbf{x}_{t_M}$

---

1113  
1114  
1115  
1116  
1117  
1118

1119   **Algorithm 8** MR Sampler-ODE-d-2.

---

1120   **Require:** initial value  $\mathbf{x}_T = \boldsymbol{\mu} + \sigma_\infty \boldsymbol{\epsilon}$ , time steps  $\{t_i\}_{i=0}^M$ , data prediction model  $\mathbf{x}_\theta$ . Denote  
1121     $h_i := \lambda_{t_i} - \lambda_{t_{i-1}}$  for  $i = 1, \dots, M$ .

1122   1:  $\mathbf{x}_{t_0} \leftarrow \mathbf{x}_T$ . Initialize an empty buffer  $Q$ .

1123   2:  $Q \xleftarrow{\text{buffer}} \mathbf{x}_\theta(\mathbf{x}_{t_0}, t_0)$

1124   3:  $\mathbf{x}_{t_1} = \frac{\sigma_{t_1}}{\sigma_{t_0}} \mathbf{x}_{t_0} + \boldsymbol{\mu} \left(1 - \frac{\sigma_{t_1}}{\sigma_{t_0}} + \frac{\sigma_{t_1}}{\sigma_{t_0}} \alpha_{t_0} - \alpha_{t_1}\right) + \alpha_{t_1} (1 - e^{-h_1}) \mathbf{x}_\theta(\mathbf{x}_{t_0}, t_0)$

1125   4:  $Q \xleftarrow{\text{buffer}} \mathbf{x}_\theta(\mathbf{x}_{t_1}, t_1)$

1126   5: **for**  $i \leftarrow 2$  to  $M$  **do**

1127    6:  $\mathbf{x}_{t_i} = \frac{\sigma_{t_i}}{\sigma_{t_{i-1}}} \mathbf{x}_{t_{i-1}} + \boldsymbol{\mu} \left(1 - \frac{\sigma_{t_i}}{\sigma_{t_{i-1}}} + \frac{\sigma_{t_i}}{\sigma_{t_{i-1}}} \alpha_{t_{i-1}} - \alpha_{t_i}\right) + \alpha_{t_i} (1 - e^{-h_i}) \mathbf{x}_\theta(\mathbf{x}_{t_{i-1}}, t_{i-1}) +$   
1128     $\alpha_{t_i} (h_i - 1 + e^{-h_i}) \frac{\mathbf{x}_\theta(\mathbf{x}_{t_{i-1}}, t_{i-1}) - \mathbf{x}_\theta(\mathbf{x}_{t_{i-2}}, t_{i-2})}{h_{i-1}}$

1129    7: If  $i < M$ , then  $Q \xleftarrow{\text{buffer}} \mathbf{x}_\theta(\mathbf{x}_{t_i}, t_i)$

1130   8: **end for**

1131   9: **return**  $\mathbf{x}_{t_M}$

---

## 1134 D DETAILS ABOUT EXPERIMENTS

### 1135 D.1 DETAILS ABOUT DATASETS

1136 We list details about the used datasets in 10 image restoration tasks in Table 5.

1140 Task name	1141 Dataset name	1142 Reference	1143 Number of testing images
Blurry	GoPro	Nah et al. (2017)	1111
Hazy	RESIDE-6k	Qin et al. (2020a)	1000
JPEG-compressing	DIV2K, Flickr2K and LIVE1	Agustsson & Timofte (2017), Timofte et al. (2017), Sheikh (2005)	29
Low-light	LOL	Wei et al. (2018)	15
Noisy	DIV2K, Flickr2K and CBSD68	Agustsson & Timofte (2017), Timofte et al. (2017), Martin et al. (2001)	68
Raindrop	RainDrop	Qian et al. (2018)	58
Rainy	Rain100H	(Yang et al., 2017)	100
Shadowed	SRD	(Qu et al., 2017)	408
Snowy	Snow100K-L	(Liu et al., 2018)	601
Inpainting	CelebaHQ	(Lugmayr et al., 2022)	100

1144 Table 5: Details about the used datasets in 10 image restoration tasks

### 1153 D.2 DETAILS ON THE NEURAL NETWORK ARCHITECTURE

1154 In this section, we describe the neural network architecture used in experiments. We follow the  
 1155 framework of Luo et al. (2024a), an image restoration model designed to address multiple degra-  
 1156 dation problems simultaneously without requiring prior knowledge of the degradation. The diffusion  
 1157 model in Luo et al. (2024a) is derived from Luo et al. (2023c), and its neural network architecture  
 1158 is based on *NAFNet*. NAFNet builds upon the U-Net architecture by replacing traditional activa-  
 1159 tion functions with *SimpleGate* and incorporating an additional multi-layer perceptron to manage  
 1160 channel scaling and offset parameters for embedding temporal information into the attention and  
 1161 feedforward layers. For further details, please refer to Section 4.2 in Luo et al. (2023c).

### 1163 D.3 DETAILED METRICS ON ALL TASKS

1164 We list results on four metrics for ten image restoration tasks in Table 6-15.

NFE	Method	LPIPS↓	FID↓	PSNR↑	SSIM↑
100	Posterior	<b>0.0385</b>	18.35	<b>29.49</b>	<b>0.9102</b>
	Euler	0.0426	20.71	29.34	0.8981
	MR Sampler-1	0.0390	<b>18.16</b>	29.45	0.9086
	MR Sampler-2	0.0397	<b>18.81</b>	29.30	0.9055
50	Posterior	0.4238	247.0	12.85	0.6048
	Euler	0.4449	249.5	12.68	0.5800
	MR Sampler-1	<b>0.0379</b>	<b>18.03</b>	<b>29.68</b>	<b>0.9118</b>
	MR Sampler-2	0.0402	19.09	29.15	0.9046
20	Posterior	0.7130	347.4	10.19	0.2171
	Euler	0.7257	344.3	10.16	0.2073
	MR Sampler-1	<b>0.0383</b>	<b>18.29</b>	<b>30.05</b>	<b>0.9172</b>
	MR Sampler-2	0.0408	19.13	28.98	0.9032
10	Posterior	0.8097	374.1	9.802	0.1339
	Euler	0.8154	381.1	9.786	0.1305
	MR Sampler-1	<b>0.0401</b>	<b>18.46</b>	<b>30.61</b>	<b>0.9229</b>
	MR Sampler-2	0.0437	19.29	28.48	0.8996
5	Posterior	0.8489	385.6	9.599	0.1057
	Euler	0.8525	384.7	9.587	0.1042
	MR Sampler-1	<b>0.0428</b>	<b>20.00</b>	<b>31.03</b>	<b>0.9262</b>
	MR Sampler-2	0.0529	24.02	28.35	0.8930

1183 Table 6: Image inpainting.

NFE	Method	LPIPS↓	FID↓	PSNR↑	SSIM↑
100	Posterior	0.0614	21.42	27.43	<b>0.8763</b>
	Euler	0.0683	23.27	27.09	0.8577
	MR Sampler-1	<b>0.0608</b>	<b>21.30</b>	<b>27.45</b>	0.8754
	MR Sampler-2	0.0626	21.47	27.18	0.8691
50	Posterior	0.2374	72.04	21.35	0.7037
	Euler	0.2730	76.02	21.02	0.6676
	MR Sampler-1	<b>0.0602</b>	<b>20.91</b>	<b>27.63</b>	<b>0.8803</b>
	MR Sampler-2	0.0628	21.85	27.08	0.8685
20	Posterior	0.6622	123.8	16.42	0.3546
	Euler	0.6861	126.0	16.23	0.3431
	MR Sampler-1	<b>0.0601</b>	<b>21.32</b>	<b>28.07</b>	<b>0.8903</b>
	MR Sampler-2	0.0650	22.34	26.89	0.8645
10	Posterior	0.8013	138.5	14.76	0.2694
	Euler	0.8164	140.4	14.64	0.2640
	MR Sampler-1	<b>0.0608</b>	<b>22.26</b>	<b>28.50</b>	<b>0.8992</b>
	MR Sampler-2	0.0698	23.92	26.49	0.8573
5	Posterior	0.8590	145.8	13.92	0.2318
	Euler	0.8680	145.8	13.85	0.2290
	MR Sampler-1	<b>0.0611</b>	23.29	<b>28.89</b>	<b>0.9065</b>
	MR Sampler-2	0.0628	<b>21.95</b>	27.06	0.8718

1184 Table 7: Snowy image restoration.

NFE	Method	LPIPS↓	FID↓	PSNR↑	SSIM↑
100	Posterior	<b>0.0970</b>	20.14	<b>27.84</b>	<b>0.8391</b>
	Euler	0.1129	20.30	27.59	0.8112
	MR Sampler-1	0.0984	<b>20.03</b>	27.73	0.8370
	MR Sampler-2	0.0989	20.69	27.44	0.8329
50	Posterior	0.6119	101.8	18.29	0.4720
	Euler	0.6985	114.2	17.80	0.4123
	MR Sampler-1	<b>0.0978</b>	20.90	<b>27.92</b>	<b>0.8409</b>
	MR Sampler-2	0.1006	<b>20.74</b>	27.20	0.8310
20	Posterior	1.043	187.2	14.73	0.2049
	Euler	1.065	192.9	14.56	0.1955
	MR Sampler-1	<b>0.0954</b>	<b>19.79</b>	<b>28.31</b>	<b>0.8505</b>
	MR Sampler-2	0.1014	20.93	27.17	0.8299
10	Posterior	1.122	208.4	13.67	0.1525
	Euler	1.133	209.7	13.57	0.1484
	MR Sampler-1	<b>0.0956</b>	<b>19.87</b>	<b>28.67</b>	<b>0.8554</b>
	MR Sampler-2	0.1044	21.85	26.99	0.8276
5	Posterior	1.155	218.9	13.12	0.1298
	Euler	1.161	221.4	13.06	0.1278
	MR Sampler-1	<b>0.0964</b>	<b>20.16</b>	<b>28.90</b>	<b>0.8601</b>
	MR Sampler-2	0.2203	36.69	23.73	0.6690

Table 8: Shadowed image restoration.

NFE	Method	LPIPS↓	FID↓	PSNR↑	SSIM↑
100	Posterior	<b>0.0594</b>	<b>25.58</b>	29.14	<b>0.8704</b>
	Euler	0.0725	28.80	28.77	0.8473
	MR Sampler-1	<b>0.0594</b>	30.53	<b>29.15</b>	0.8679
	MR Sampler-2	0.0616	27.33	28.92	0.8614
50	Posterior	0.4418	183.1	16.41	0.4903
	Euler	0.4560	185.2	16.24	0.4729
	MR Sampler-1	<b>0.0586</b>	30.73	<b>29.34</b>	<b>0.8730</b>
	MR Sampler-2	0.0620	<b>27.65</b>	28.85	0.8602
20	Posterior	0.6865	293.6	12.54	0.2464
	Euler	0.6943	299.0	12.49	0.2402
	MR Sampler-1	<b>0.0604</b>	31.19	<b>29.81</b>	<b>0.8845</b>
	MR Sampler-2	0.0635	<b>27.79</b>	28.60	0.8559
10	Posterior	0.7972	323.0	11.50	0.1755
	Euler	0.8043	330.8	11.46	0.1724
	MR Sampler-1	<b>0.0659</b>	31.66	<b>30.28</b>	<b>0.8943</b>
	MR Sampler-2	0.0678	<b>29.54</b>	28.09	0.8483
5	Posterior	0.8663	332.4	10.96	0.1450
	Euler	0.8714	332.5	10.94	0.1435
	MR Sampler-1	0.0729	32.06	<b>30.68</b>	<b>0.9029</b>
	MR Sampler-2	<b>0.0637</b>	<b>26.92</b>	28.82	0.8685

Table 9: Rainy image restoration.

NFE	Method	LPIPS↓	FID↓	PSNR↑	SSIM↑
100	Posterior	0.0443	<b>19.70</b>	<b>30.05</b>	<b>0.8910</b>
	Euler	0.0634	24.19	29.31	0.8438
	MR Sampler-1	<b>0.0437</b>	19.94	29.91	0.8852
	MR Sampler-2	0.0454	21.35	29.55	0.8768
50	Posterior	0.4289	100.1	23.19	0.4663
	Euler	0.5011	111.6	22.35	0.4106
	MR Sampler-1	<b>0.0428</b>	<b>19.14</b>	<b>30.07</b>	<b>0.8914</b>
	MR Sampler-2	0.0459	20.50	29.40	0.8764
20	Posterior	0.8873	190.8	17.37	0.1925
	Euler	0.9082	194.1	17.10	0.1839
	MR Sampler-1	<b>0.0439</b>	<b>19.31</b>	<b>30.44</b>	<b>0.9025</b>
	MR Sampler-2	0.0470	21.08	29.34	0.8745
10	Posterior	0.9884	215.5	15.67	0.1419
	Euler	0.9993	213.1	15.52	0.1381
	MR Sampler-1	<b>0.0466</b>	<b>20.60</b>	<b>30.77</b>	<b>0.9114</b>
	MR Sampler-2	0.0485	22.17	29.37	0.8779
5	Posterior	1.030	226.3	14.82	0.1209
	Euler	1.037	226.4	14.74	0.1190
	MR Sampler-1	<b>0.0497</b>	<b>21.18</b>	<b>31.04</b>	<b>0.9175</b>
	MR Sampler-2	0.0733	28.26	28.03	0.8369

Table 10: Raindrop image restoration.

NFE	Method	LPIPS↓	FID↓	PSNR↑	SSIM↑
100	Posterior	0.1694	65.79	<b>25.97</b>	<b>0.7267</b>
	Euler	0.2719	68.69	24.28	0.5686
	MR Sampler-1	0.1629	<b>59.12</b>	<b>25.97</b>	0.7244
	MR Sampler-2	<b>0.1586</b>	64.02	25.67	0.7126
50	Posterior	0.7713	135.7	18.19	0.2763
	Euler	0.8060	143.5	17.74	0.2615
	MR Sampler-1	0.1680	65.14	<b>26.20</b>	<b>0.7330</b>
	MR Sampler-2	<b>0.1615</b>	<b>64.24</b>	25.61	0.7127
20	Posterior	0.9941	181.6	14.76	0.1821
	Euler	1.006	188.3	14.61	0.1781
	MR Sampler-1	0.1872	71.31	<b>26.68</b>	<b>0.7494</b>
	MR Sampler-2	<b>0.1695</b>	<b>64.90</b>	25.46	0.7098
10	Posterior	1.057	202.6	13.59	0.1550
	Euler	1.063	207.0	13.51	0.1529
	MR Sampler-1	0.2043	79.28	<b>27.13</b>	<b>0.7628</b>
	MR Sampler-2	<b>0.1853</b>	<b>70.19</b>	25.09	0.6984
5	Posterior	1.087	213.5	13.00	0.1419
	Euler	1.091	218.6	12.96	0.1408
	MR Sampler-1	<b>0.2046</b>	80.45	<b>27.51</b>	<b>0.7743</b>
	MR Sampler-2	0.3178	<b>73.93</b>	24.32	0.5485

Table 11: Noisy image restoration.

1223  
1224  
1225  
1226  
1227  
1228  
1229  
1230  
1231  
1232  
1233  
1234  
1235  
1236  
1237  
1238  
1239  
1240  
1241

NFE	Method	LPIPS↓	FID↓	PSNR↑	SSIM↑
100	Posterior	0.0796	34.70	<b>23.84</b>	<b>0.8496</b>
	Euler	0.1014	37.46	23.27	0.8027
	MR Sampler-1	<b>0.0774</b>	32.91	23.80	0.8451
	MR Sampler-2	0.0789	<b>32.91</b>	23.59	0.8394
50	Posterior	0.6572	151.3	9.490	0.2746
	Euler	0.7517	176.7	9.402	0.2340
	MR Sampler-1	<b>0.0784</b>	34.45	23.51	<b>0.8476</b>
	MR Sampler-2	0.0786	<b>32.85</b>	<b>23.52</b>	0.8382
20	Posterior	1.288	390.1	8.211	0.0648
	Euler	1.297	396.8	8.212	0.0625
	MR Sampler-1	<b>0.0791</b>	35.28	<b>24.22</b>	<b>0.8586</b>
	MR Sampler-2	0.0792	<b>32.80</b>	23.63	0.8399
10	Posterior	1.351	432.2	8.130	0.0476
	Euler	1.354	424.2	8.136	0.0467
	MR Sampler-1	<b>0.0831</b>	41.10	<b>24.04</b>	<b>0.8619</b>
	MR Sampler-2	0.0841	<b>36.53</b>	23.22	0.8398
5	Posterior	1.371	453.0	8.114	0.0408
	Euler	1.372	447.2	8.118	0.0405
	MR Sampler-1	0.0860	41.81	24.02	<b>0.8676</b>
	MR Sampler-2	<b>0.0782</b>	<b>33.98</b>	<b>24.13</b>	0.8507

Table 12: Low-light image restoration.

NFE	Method	LPIPS↓	FID↓	PSNR↑	SSIM↑
100	Posterior	0.1702	45.77	25.78	<b>0.7380</b>
	Euler	0.2949	56.99	23.84	0.5398
	MR Sampler-1	0.1636	<b>43.67</b>	<b>25.81</b>	0.7362
	MR Sampler-2	<b>0.1555</b>	44.58	25.46	0.7220
50	Posterior	0.6494	103.7	19.34	0.2908
	Euler	0.7035	113.7	18.62	0.2659
	MR Sampler-1	0.1734	47.09	<b>26.06</b>	<b>0.7470</b>
	MR Sampler-2	<b>0.1567</b>	<b>45.56</b>	25.41	0.7224
20	Posterior	0.8252	140.6	16.44	0.1988
	Euler	0.8477	144.5	16.19	0.1921
	MR Sampler-1	0.1993	51.43	<b>26.58</b>	<b>0.7649</b>
	MR Sampler-2	<b>0.1675</b>	<b>47.36</b>	25.33	0.7235
10	Posterior	0.8723	158.9	15.49	0.1738
	Euler	0.8859	159.9	15.34	0.1701
	MR Sampler-1	0.2183	57.83	<b>26.98</b>	<b>0.7771</b>
	MR Sampler-2	<b>0.1871</b>	<b>51.25</b>	25.08	0.7197
5	Posterior	0.8941	163.6	14.99	0.1615
	Euler	0.9013	162.0	14.91	0.1596
	MR Sampler-1	<b>0.2281</b>	<b>59.17</b>	<b>27.28</b>	<b>0.7853</b>
	MR Sampler-2	0.3751	62.60	23.15	0.4797

Table 13: JPEG image restoration.

NFE	Method	LPIPS↓	FID↓	PSNR↑	SSIM↑
100	Posterior	<b>0.0211</b>	<b>4.755</b>	30.37	<b>0.9485</b>
	Euler	0.0358	6.182	29.95	0.9319
	MR Sampler-1	0.0219	4.826	<b>30.42</b>	0.9462
	MR Sampler-2	0.0230	4.978	30.26	0.9431
50	Posterior	0.3994	35.47	15.34	0.5808
	Euler	0.4745	42.70	15.16	0.5160
	MR Sampler-1	<b>0.0211</b>	<b>4.737</b>	<b>30.49</b>	<b>0.9484</b>
	MR Sampler-2	0.0233	4.993	30.19	0.9427
20	Posterior	0.9911	114.0	12.81	0.1832
	Euler	1.012	118.5	12.71	0.1752
	MR Sampler-1	<b>0.0200</b>	<b>4.682</b>	<b>30.63</b>	<b>0.9534</b>
	MR Sampler-2	0.0240	5.077	30.06	0.9409
10	Posterior	1.116	144.0	11.94	0.1261
	Euler	1.128	147.3	11.87	0.1228
	MR Sampler-1	<b>0.0197</b>	<b>4.785</b>	<b>30.80</b>	<b>0.9579</b>
	MR Sampler-2	0.0246	5.228	29.65	0.9372
5	Posterior	1.162	159.1	11.47	0.1042
	Euler	1.168	161.2	11.43	0.1026
	MR Sampler-1	<b>0.0205</b>	<b>4.926</b>	<b>30.56</b>	<b>0.9604</b>
	MR Sampler-2	0.0228	5.174	29.65	0.9416

Table 14: Hazy image restoration.

NFE	Method	LPIPS↓	FID↓	PSNR↑	SSIM↑
100	Posterior	0.1249	<b>14.48</b>	<b>27.48</b>	<b>0.8442</b>
	Euler	0.1404	16.06	27.16	0.8179
	MR Sampler-1	<b>0.1239</b>	14.61	27.46	0.8419
	MR Sampler-2	0.1248	14.61	27.30	0.8365
50	Posterior	0.5112	45.13	24.41	0.5571
	Euler	0.5739	61.21	23.79	0.4957
	MR Sampler-1	0.244	<b>14.47</b>	<b>27.59</b>	<b>0.8461</b>
	MR Sampler-2	<b>0.1251</b>	14.62	27.24	0.8360
20	Posterior	1.069	117.8	18.20	0.1717
	Euler	1.089	120.8	17.94	0.1637
	MR Sampler-1	0.1287	14.92	<b>27.85</b>	<b>0.8544</b>
	MR Sampler-2	<b>0.1266</b>	<b>14.82</b>	27.13	0.8337
10	Posterior	1.187	141.9	16.11	0.1136
	Euler	1.197	143.7	15.96	0.1104
	MR Sampler-1	0.1356	15.65	<b>28.10</b>	<b>0.8613</b>
	MR Sampler-2	<b>0.1300</b>	<b>15.51</b>	26.88	0.8295
5	Posterior	1.228	155.3	15.08	0.0922
	Euler	1.234	157.3	15.00	0.0907
	MR Sampler-1	0.1422	16.32	<b>28.31</b>	<b>0.8668</b>
	MR Sampler-2	<b>0.1248</b>	<b>14.20</b>	26.92	0.8354

Table 15: Motion-blurry image restoration.

#### D.4 DETAILS ON NUMERICAL STABILITY AT LOW NFEs

We have included further details regarding numerical stability at 5 NFEs to complement the experiments presented in Section 5.3. As illustrated in Figure 5, when the NFE is relatively low, the convergence rate of noise prediction at each step does not exceed 40%, which results in sampling collapse. In contrast, during the final 1 or 2 steps, the convergence rate of data prediction approaches nearly 100%.

#### D.5 WALL CLOCK TIME

We measured the wall clock time in our experiments on a single NVIDIA A800 GPU. The average wall clock time per image of two representative tasks (low-light and motion-blurry image restoration) are reported in Table 16 and 17.

#### D.6 PRESENTATION OF SAMPLING RESULTS

We present the sampling results for all image restoration tasks in Figure 6 and 7. We choose one image for each task.

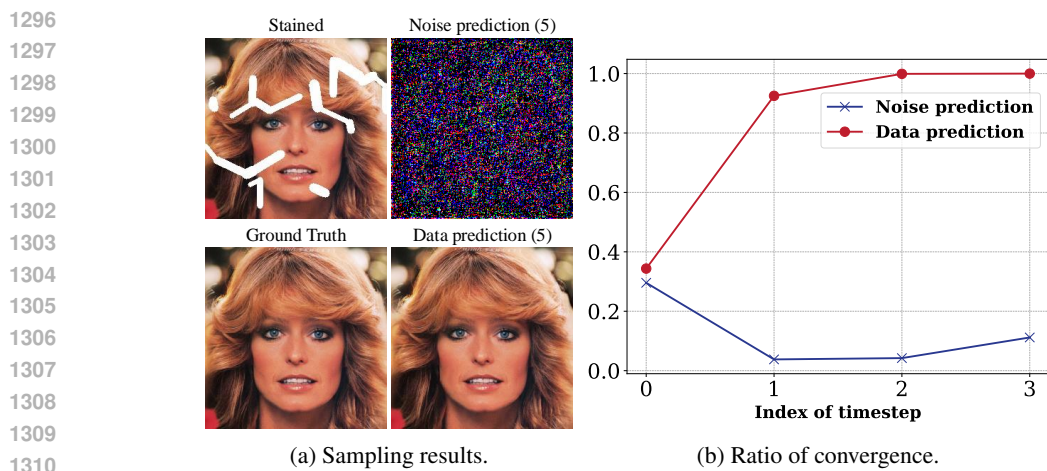


Figure 5: **Convergence of noise prediction and data prediction at 5 NFEs.** In (a), we choose a stained image for example. The numbers in parentheses indicate the NFE. In (b), we illustrate the ratio of components of neural network output that satisfy the Taylor expansion convergence requirement.

Table 16: Wall clock time on the Low-light dataset.

NFE	Method	Time(s)↓
100	Posterior Sampling	17.19
	MR Sampler-2	17.83
50	Posterior Sampling	8.605
	MR Sampler-2	8.439
20	Posterior Sampling	3.445
	MR Sampler-2	3.285
10	Posterior Sampling	1.727
	MR Sampler-2	1.569
5	Posterior Sampling	0.8696
	MR Sampler-2	0.7112

Table 17: Wall clock time on the Motion-blurry dataset.

NFE	Method	Time(s)↓
100	Posterior Sampling	82.04
	MR Sampler-2	81.16
50	Posterior Sampling	41.23
	MR Sampler-2	40.18
20	Posterior Sampling	16.44
	MR Sampler-2	15.59
10	Posterior Sampling	8.212
	MR Sampler-2	7.413
5	Posterior Sampling	4.133
	MR Sampler-2	3.294

## E SELECTION OF THE OPTIMAL NFE

In practice, sampling quality is expected to degrade as the NFE decreases, which requires us to make a trade-off between sampling quality and efficiency. From the perspective of reverse-time SDE and PF-ODE, the estimation error of the solution plays a critical role in determining the sampling quality. This estimation error is primarily influenced by  $h_{max} = \max_{1 \leq i \leq M} \lambda_i - \lambda_{i-1} = \mathcal{O}(\frac{1}{M})$ , where  $M$  represents the NFE. During sampling, the noise schedule must be designed in advance, which also determines the  $\lambda$  schedule. Since  $\lambda_i$  is monotonically increasing, a larger NFE results in a smaller  $h_{max}$ , thereby reducing the estimation error and improving sampling quality. However, different sampling algorithms exhibit varying convergence rates. Experimental results show that the MR Sampler (our method) can achieve a good score with as few as 5 NFEs, whereas posterior sampling and Euler discretization fail to converge even with 50 NFEs.

Specifically, we conducted experiments on the snowy dataset with low NFE settings, and the results are presented in Table 18. The sampling quality remains largely stable for NFE values larger than 10, gradually deteriorates when the NFE is below 10, and collapses entirely when NFE is reduced to 2. Based on our experience, we recommend using 10–20 NFEs, which provides a reasonable trade-off between efficiency and performance.

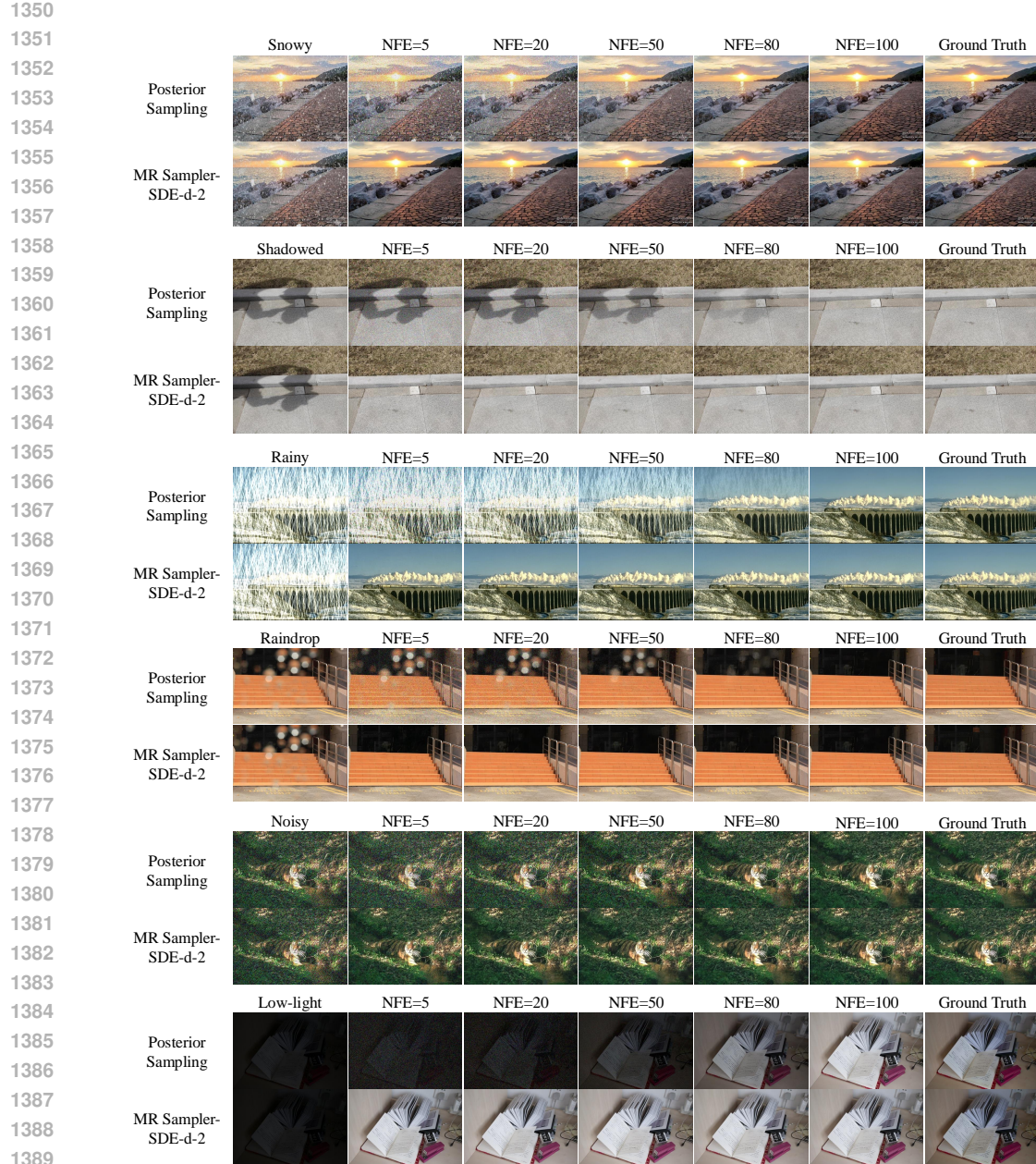
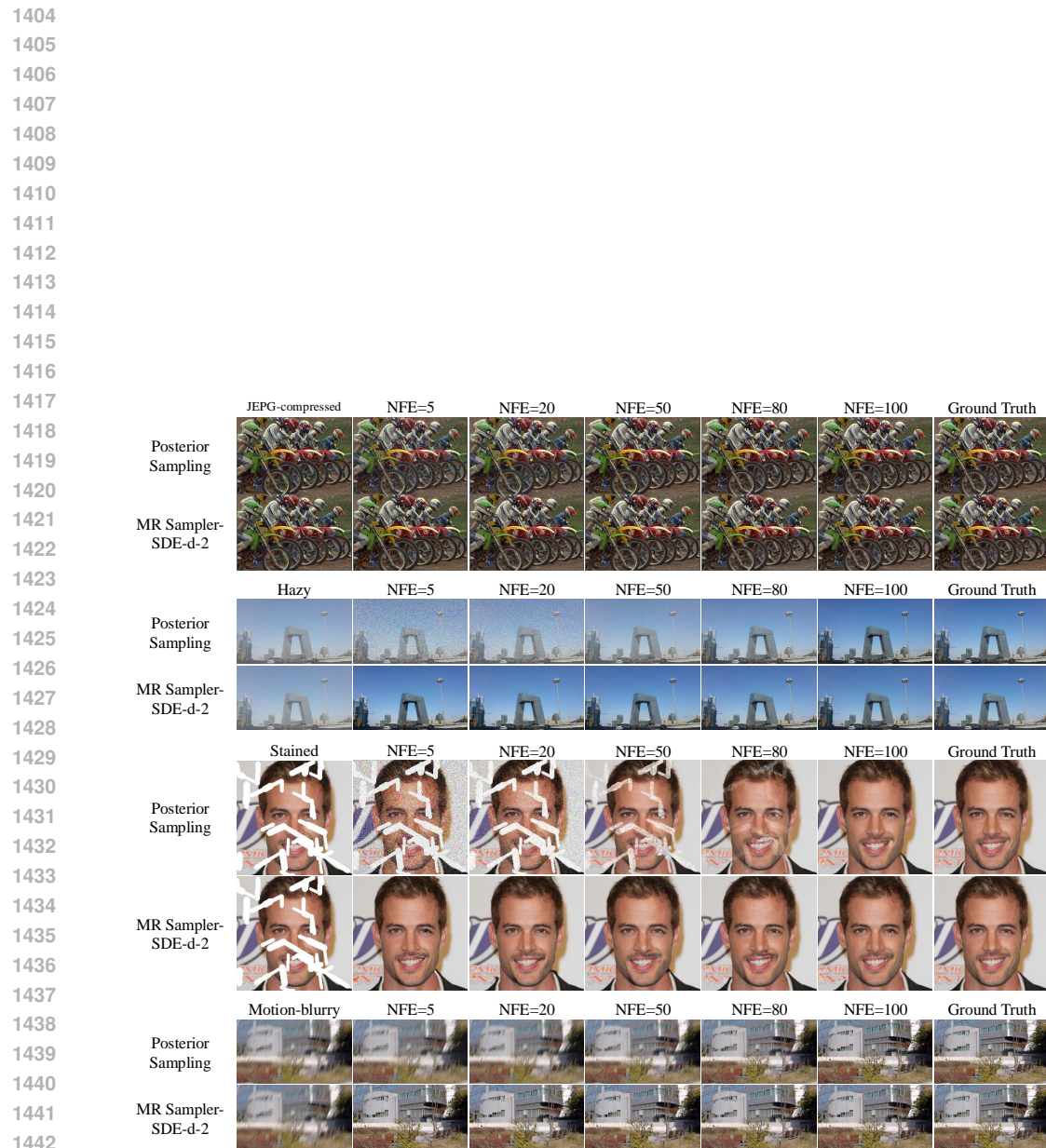


Figure 6: Comparisons between *posterior sampling* and *MR Sampler-SDE-d-2* on snowy, shadowed, rainy, raindrop, noisy and low-light datasets.

Table 18: Results of MR Sampler-SDE-2 with data prediction and uniform  $\lambda$  on the snowy dataset.

NFE	100	50	20	10	8	6	5	4	2
LPIPS $\downarrow$	0.0626	0.0628	0.0650	0.0698	0.0725	0.0744	0.0628	0.1063	1.422
FID $\downarrow$	21.47	21.85	22.34	23.92	24.81	25.60	21.95	30.18	421.1
PSNR $\uparrow$	27.18	27.08	26.89	26.49	26.61	26.40	27.06	25.38	6.753
SSIM $\uparrow$	0.8691	0.8685	0.8645	0.8573	0.8462	0.8407	0.8718	0.7640	0.0311



1443      **Figure 7: Comparisons between *posterior sampling* and *textit{MR Sampler-SDE-d-2}* on JPEG-  
1444 compressed, hazy, inpainting and motion-blurry datasets.**  
1445

1446  
1447  
1448  
1449  
1450  
1451  
1452  
1453  
1454  
1455  
1456  
1457